The Stimulus-Response Transformation of the SAI Tactile Afferent is Modulated by the Number and Arrangement of Merkel Cells in its Compound End Organ

---

A dissertation presented to

the faculty of the School of Engineering and Applied Science

University of Virginia

In partial fulfillment

of the requirements for the degree of

Doctor of Philosophy in Systems Engineering

by

Daine R. Lesniak

May, 2013

Approval Sheet

This dissertation is submitted in partial fulfillment of the requirements for the degree of
Doctor of Philosophy in Systems Engineering

_____

Daine R. Lesniak
Author

This dissertation has been read and approved by the examining committee:

_____

Dr. Gregory J. Gerling
Dissertation Advisor

_____

Dr. Donald E. Brown
Committee Chair

_____

Dr. Gerard P. Learmonth, Sr

_____

Dr. Jason A. Papin

_____

Dr. Ellen A. Lumpkin

Accepted for the school of Engineering and Applied Science:

_____

Dean, School of Engineering and Applied Science
May 2013

Slowly adapting type I (SAI) afferents are gentle touch receptors that respond to a robust range of indentation with well-defined receptive fields, making them vital to discriminating shapes and textures. Despite its importance to our sense of touch, the SAI afferent's transformation of skin indentation to neural signals is not fully understood. In particular, it is not known how the SAI afferent response is influenced by its end organ, a tree like structure where the afferent branches repeatedly to terminate at a number of sensory Merkel cells, nor is it known which aspects of this natural compound sensor might inform the design of artificial sensors. To address these gaps, this work develops models representing SAI end organs embedded in skin with finite element modeling (FEM), fitted functions, probabilistic noise distributions, and differential equations*. The models can be configured to represent specific end-organ structures with a reconfigurable network of transduction functions, each representing a cluster of Merkel cell-neurite complexes providing receptor currents, and leaky integrate and fire models representing spike initiation zones. This approach circumvents the inability to obtain recordings of neural spike trains and reconstructions of end organ structure from the same SAI afferent. Simulation studies using these models indicate that 1) the grouping of Merkel cells to spike initiation zones impacts the SAI afferent response, and can obscure the impact of Merkel cell count, 2) while an increase in Merkel cells grouped to spike initiation zones – as the end organ remodels over the hair cycle – causes an increase in firing rate, a counteracting increase in skin thickness may help maintain the magnitude of the neural response, and 3) when mimicking the end organ to inform artificial compound sensors, the mechanism of resetting between multiple spike encoders is essential to providing durability to transducer failures, and this durability increases with the number of spike encoders but decreases with the number of transducers associated with each spike encoder.*

Table of Contents

List of Figures:

List of Equations:

List of Tables:

1. Overview and Objectives

The sense of touch is vital to human health and independent living. Without the sense of touch, it is difficult to perform tasks such as feeding oneself. The tactile perception of shape and pressure, essential to such tasks, is facilitated in part by the slowly adapting type I (SAI) afferent. Despite its importance to tactile perception, the link between the SAI afferent's morphology and the transformation of skin indentation to neural spikes is not fully understood. Specifically, it is not yet known how the configuration of the SAI afferent's compound end organ, where the afferent branches to contact multiple sensory Merkel cells, influences the pattern of neural spikes elicited. The work herein hypothesizes that the number and grouping of Merkel cells to spike initiation zones in the SAI end organ modulates spike firing. This central hypothesis is supported by three aims.

The first aim seeks to account for differences in responses between SAI afferents as a function of end organ structure. To do so, a reconfigurable model of the SAI end organ is developed by combining finite element modeling (FEM), fitted functions, probabilistic noise distributions, and differential equations. These techniques allow modeling the transformation of skin indentation to strain energy density (SED), of SED to membrane current by receptor transduction, and of current to spike times by spike initiation. Models are configured to match representative groupings of Merkel cells to spike initiation zones as observed in SAI end-organ reconstructions, and modeled spike responses are fit against SAI spike recordings from mice using response surface methodology with space filling designs. After constraining prototypical end organ models, computational experiments are run to examine the impact of both the number of Merkel cells and the grouping of Merkel cells to spike initiation zones within the end organ. These experiments revealed that both the number of Merkel cells and the grouping of Merkel cells to spike initiation zones influences the SAI afferent response, in terms of both

absolute firing rates and sensitivity, and that the grouping of Merkel cells to spike initiation zones can obscure the impact of Merkel cell count.

The second aim examines the impact of end organ remodeling on the SAI afferent stimulus-response transformation during the hair cycle, and determines if increases in skin thickness can counteract the effect of increased Merkel-cell counts associated with remodeling. To do so, the model developed in aim 1 was configured for representative end organs of active and rest stages of the hair cycle, and finite element models were utilized covering the range of skin thicknesses for the same period of weeks. Computational experiments demonstrated the feasibility of increases in skin thickness counteracting the impact of increasing Merkel-cell counts as the end organ remodels, suggesting the interaction of skin and end organ may maintain homeostasis with respect to the SAI afferent stimulus-response transformations.

In addition to increasing our understanding of tactile sensing in the biology, this work sought to extend this knowledge to engineered systems. To do so, the third aim examines how mimicking aspects of the SAI afferent's end organ, such as multiple transducers (Merkel cell-neurite complexes) and resetting between multiple spike encoders, may lead to more durable artificial sensors. Compound spiking sensors are modeled as a network of transduction functions and leaky integrate and fire models, using force transducer readings from an existing spiking sensor system. Simulations with this model reveal that resetting between multiple spike encoders allows a stable stimulus-response transformation as a number of transducers fail. Additionally, fault tree analysis indicates that compound sensor durability increases with the number of spike encoders (i.e. leaky integrate and fire model and associated transduction function), but decreases with the number of force transducers associated with each. Therefore, the most durable system invokes the use of multiple spike encoder–force transducer pairs, where spike encoders reset each other on spike initiation.

2. Background

When we touch an object, a diverse group of mechanoreceptors in our skin respond with a series of neural action potentials, referred to as spikes, which the nervous system integrates to constitute our sense of touch. For example, spikes from Pacinian corpusle (PC) afferents facilitate perception of high frequency vibration while perception of low frequency vibration and slip are mediated by rapidly adapting afferents (RA) [1]. Spikes from the slowly adapting type I (SAI) afferents, in particular, facilitate the perception of sustained pressure, edges, and curvature.

SAI end organs are tree-like structures where the afferent branches repeatedly to terminate in a few to dozens of Merkel cell-neurite complexes (Fig 2.1), and are located in touch-sensitive regions of mammalian skin, including fingertips, whiskers, and touch domes [2][3]. When an object deforms the skin's surface, mechanical distortions propagate to the end organ, located at the epidermal-dermal border, and Merkel cell-neurite complexes transform local distortions to ionic receptor currents that are then integrated by spike initiation zones. The resulting spikes then integrate along the branching structure to produce the SAI afferent response.

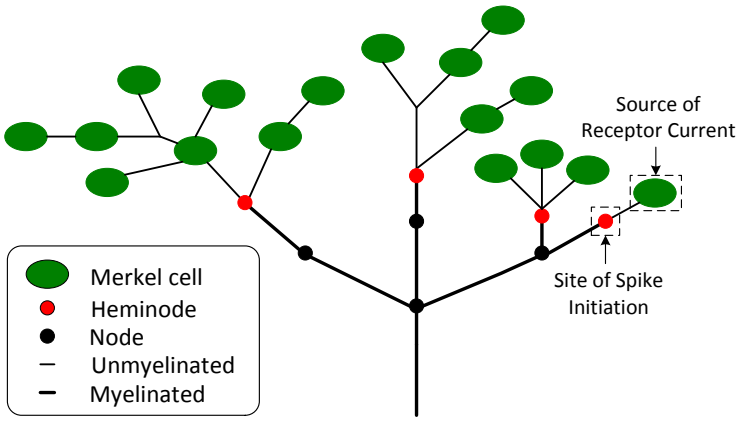

Figure 2.1: SAI end organ where the afferent branches several times before terminating in a number of Merkel cells. Current from Merkel cell – neurite complexes, where the Merkel cell is met by an unmyelinated neurite, drives spike initiation at heminodes (spike initiation zones).

Experimental approaches. Experimental approaches to studying the SAI afferent span multiple levels of tactile perception (Fig 2.2). For example, psychophysical experiments link mechanical stimuli such as points, gratings, and complex shapes with reported perceptions in human subjects [4]. Linking reported perceptions to neural signals from particular afferents has been accomplished, in part, with electrical stimulation experiments. For example, in agreement with perceptions elicited by mechanical stimulation, electrical stimulation of SAI afferents has been shown to produce the perception of sustained pressure [5]. While these approaches link mechanical stimuli and orthodromically induced neural signals to perceptions, single unit electrophysiological recordings can be used to understand how neural responses are elicited by mechanical stimuli.

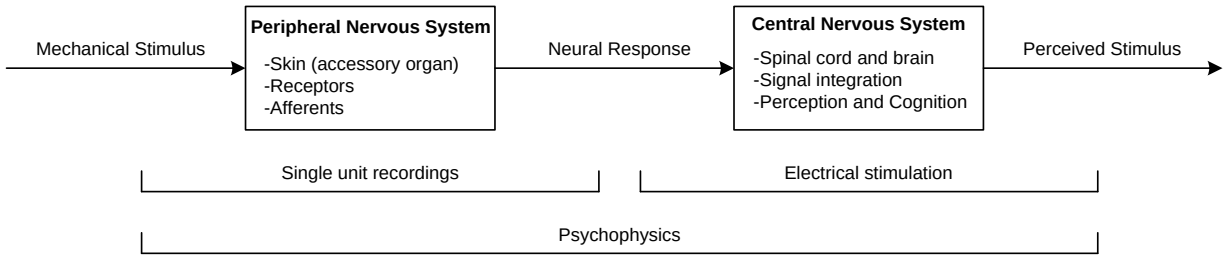

Figure 2.2: The role of the SAI afferent in touch sensation has been experimentally examined with psychophysics to link stimuli to perceptions, electrical stimulation to link neural signals to perceptions, and single-unit recordings to link mechanical stimuli to neural responses.

SAI afferent recordings in mice, a genetically and experimentally tractable mammal, are often performed using ex-vivo skin-nerve preparations [6], in which a portion of the skin containing the SAI end organ is excised with the nerve intact (Figure 2.3A), and is placed in a recording chamber allowing the skin to be maintained at body temperature and perfused with synthetic interstitial fluid. By subdividing the nerve over a differential electrode, it is possible to record spikes from single SAI afferents as controlled displacements are applied to the skin (Figure 2.3B). Although the majority of ex-vivo experiments mount the skin with the dermis facing up to aid in SIF perfusion, recent experiments with the epidermis facing up allow for more natural stimuli and accurate afferent classification [7].

Importantly, epidermis-up preparations also allow observing the number of Merkel cells in a SAI afferent's end organ with epiflourescent microscopy (Figure 2.3C). However, other end organ details such as the sites of spike initialization and the branching structure are unavailable.

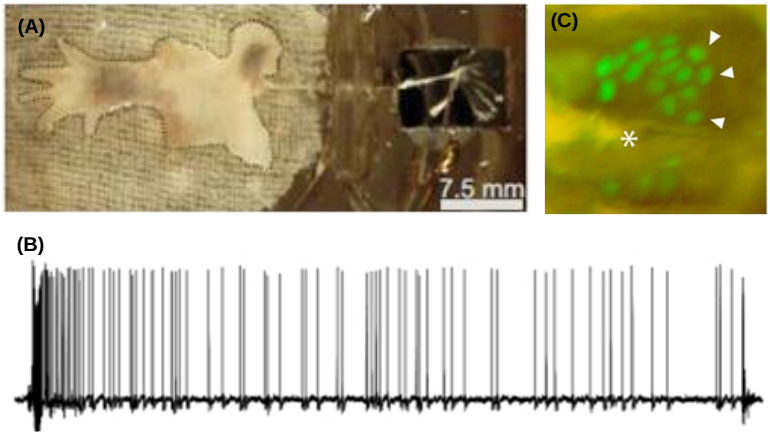

Figure 2.3: Skin-nerve preparations (A) have been used extensively in recording SAI afferent responses (B). Recent epidermis-up procedures allow the number of Merkel cells in a given SAI afferent's end organ to be obtained (C). Adapted from [7].

SAI end organ branching is available through other means, however. For example, as part of an effort to unambiguously confirm the SAI end organ as the source of slowly adapting type I responses, Woodbury and Koerber observed partial end organ branching using dye labeling and sectioning, but did not to recover the full structure, the arrangement of Merkel cells, or nodes [3]. Recently, these details have become available through 3D reconstructions using immunostaining methods, confocal imaging, and Neurolucida-based tracing [8]. These methods allow visualizing and quantifying entire SAI end organs (Fig 2.4). However, as it is not currently possible to obtain end-organ reconstructions and stimulus-response recordings for the same SAI afferent, understanding how the end organ structure and signal integration influences SAI afferent responses requires the use of modeling.

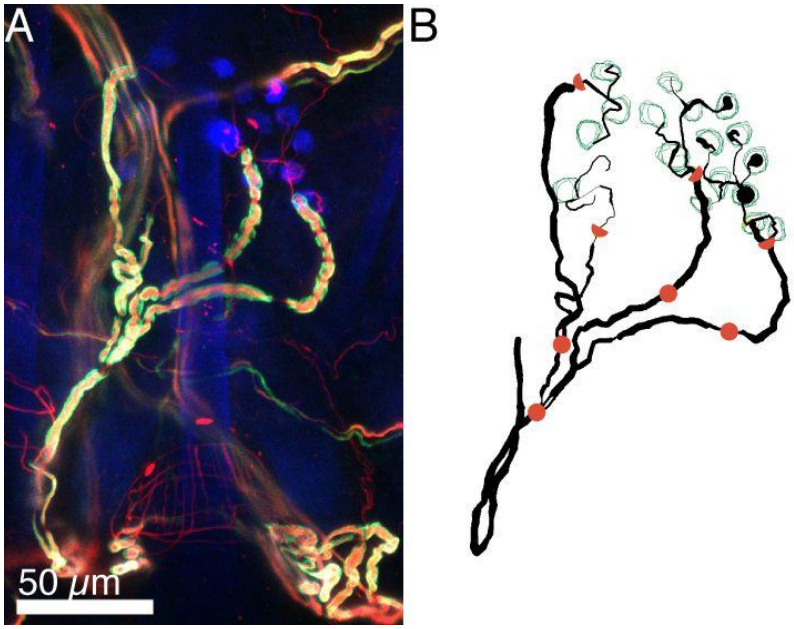

Figure 2.4: A) Projection of a immunostaining confocal image stack of a SAI end organ showing Merkel cells (Keratin 8; blue), myelinated afferents (Neurofilament-H; red), and Myelin (Myelin Basic Protein; green. B) 3D Neurolucida tracing of confocal stack in A showing SAI afferent (black), Merkel cells (green), nodes of Ranvier (red circles), heminodes (red half-circles). Adapted from [8]. © 2013, Marshall and Lumpkin. Used with permission.

Modeling approaches. Modeling SAI responses, and the underlying signaling mechanisms of the skin and neuron, has been accomplished through a variety of techniques. One technique is to fit purely empirical models to stimulus-response data. In particular, Goodwin and Wheat have developed regression functions that represent a single SAI afferent's response to specific stimuli. For example, they modeled the firing rate elicited by spherical stimuli as a two dimensional Gaussian function of sphere curvature and position relative to the receptor, multiplied by the sensitivity of the receptor [9]. Such single-receptor models have been developed and aggregated into receptor population simulations to examine the way a population might encode spheres, bars [10], and annular segments [11]. The SAI response to vibration has also been empirically modeled, where the impact of vibration frequency and amplitude on firing rate was examined with transfer functions taking power, exponential, and linear

forms [12]. Although purely empirical models have been useful, they abstract underlying physiological mechanisms and are typically tied to a predefined set of stimuli.

In contrast, skin mechanics models accept a wider range of stimuli as input, and have investigated the underlying mechanisms of the SAI's sensitivity to edges. These models represent the receptor as a stress/strain sensor embedded in an elastic matrix of skin, which is deterministically modeled with either continuum mechanics [13][14] or finite elements [15][16]. While skin is non-homogeneous, anisotropic, and exhibits complex stress-strain relationships, simplifications are made to model the elastic behavior of skin. For example, past models have used linear elastic approximations that obey Hooke's Law [16]. While fast to compute, the linear elastic approximation is valid only for small displacements (5–10%). Hyperelastic material models, such as Ogden [17][18] and Mooney-Rivlin models, are a non-linear alternative and are appropriate for larger displacements (>10%) such as those examined herein [18][19][20][21]. When a displacement is held, skin exhibits creep and relaxation, which can be captured with viscoelastic models such as Prony series [18][22]. Regardless of the exact material properties formulation used, skin models predict distributions of stress and strain throughout the skin as a result of an applied indentation or force, and then a stress or strain quantity, such as strain energy density (SED), is converted to the firing rate of a single tactile afferent with a scaling function. While the predictions of skin mechanics models closely match *in vivo* data, these models have been largely limited to predicting firing rates, rather than individual spike times.

To predict spike times, neural dynamics models can be used. Examples include the Hodgkin–Huxley model, two-dimensional reductions of the Hodgkin–Huxley model, and leaky integrate-and-fire models [23][24]. Each of these models leverages one or more differential equations that are numerically evaluated with methods such as Runge-Kutta to describe the electrical properties of excitable membranes. For example, the Hodgkin-Huxley model combines four differential equations to describe

the time and voltage dependent nature of sodium and potassium conductances, allowing for accurate reproduction of both the timing and waveforms of spikes [23]. However, the spike waveform is not of interest in coding studies and the Hodgkin-Huxley model's complexity often precludes its use in simulation [24]. Two-dimensional reductions of the Hodgkin-Huxley model, such as that derived by Izhikevich [25], decrease the required computation by approximating the Hodgkin-Huxley model with a system of two differential equations. These models are employed to efficiently reproduce diverse spiking behaviors in cortical simulations. Further abstraction yields the leaky integrate and fire model, which is composed of single differential equation.

Specific to tactile afferents, specialized leaky integrate and fire (LIF) models have been used to investigate phase locking, phase retardation, and adaptation to sinusoidal vibration [26][27][28][29][30]. These models calculate SAI membrane potential as a function of vibration frequency and magnitude, and record a spike time when the membrane potential is driven to threshold. By sampling the threshold from a normal distribution over time, noise has been incorporated into these models. Although neural dynamics and skin mechanics are tied together *in vivo,* tactile afferent neural dynamics models and skin mechanics models have largely been used in isolation.

To tie together neural dynamics and skin mechanics *in silico* as they are tied together *in vivo*, we previously developed a skin-receptor model that transforms skin indentation to spike times with three sub-transformations [31]. First, skin indentation is transformed to SED at the end organ with a two-dimensional, linear elastic finite element model of the skin. Second, SED is transformed to receptor current with a fitted function of transduction modeled after transduction in pain receptors. Finally, receptor current is transformed to spike times with a leaky integrate and fire model of neural dynamics. Although this model successfully reproduced SAI spike trains with firing rates matching those elicited by 3 and 5 mm gratings, it does not account for the branching SAI end organ with its multiple sites of spike

initiation. Therefore, a more detailed model of the SAI end organ must be developed to understand how end organ structure modulates the SAI afferent response.

3. The Arrangement of Merkel Cells in the SAI Afferent End Organ Governs its Response Magnitude and Sensitivity

Although differences in touch-sensitivity between SAI afferents are well known, the biological basis of these differences is currently unknown. Here, we seek to account for differences in SAI afferent responsiveness and supra-threshold sensitivity by the SAI afferent's end-organ structure, specifically the grouping of Merkel cell-neurite complexes to spike initiation zones. We constructed computational models combining a finite element analysis of the skin with a reconfigurable network composed of fitted functions of receptor current transduction and leaky integrate and fire models of spike initiation. This reconfigurable network allows for simulating differences in end-organ structure, in particular the allocation and connectivity of Merkel cells to spike initiation zones. Results suggest that firing rate increases with the number of Merkel-cells, but that this effect can be obscured by the grouping of Merkel-cells to spike initiation zones. For example, an increase from 17 to 24 Merkel cells causes the firing rate to increase 21% when Merkel cells were distributed more evenly {8, 6, 5, 5}, in contrast to the 39% increase when Merkel cells were skewed toward larger groups {8, 8, 7, 1}. When the total number of Merkel cells is held constant, firing rates increased an average of 7.2% per Merkel cell as Merkel cells were shifted to the largest group, and an average of 2.8% per Merkel cell as Merkel cells were shifted to the second largest group. This explains how end organs with more Merkel cells may be less sensitive than end organs with fewer, for example a model configured with 12 Merkel cells and a Merkel-cell grouping of {10, 1, 1} is 50.2 spikes/s/mm more sensitive than a model configured with 20 Merkel cells and a Merkel-cell grouping of {4, 4, 4, 4, 4}. Therefore, this work indicates that the rates of neural spike firing, as well as sensitivity (i.e. the slope of the displacement-firing rate transformation), depend on both the number of Merkel cells per afferent as well as the grouping of Merkel cells per spike initiation zone.

3.1 Introduction

There is a great deal of variation in firing rates from different SAI afferents for similar stimuli, both in overall responsiveness and sensitivity, and these differences have been observed across stimulation modalities. For example, sensitivity differences have been observed for vibrating edges [32] and gratings [33], as well as spheres [9], gapped bars [10], and annular segments [11]. Furthermore, differences in sensitivity between afferents may impact how a population of afferents is recruited [34]. Although of great interest, these differences have yet to be attributed to a particular biological variation, such as skin mechanics [35], the number of Merkel cell-neurite complexes innervated by an SAI afferent [36][37] [38], or the structure of the SAI afferent's end organ [8].

As it is not possible to obtain electrophysiological recordings and end organ reconstructions for the same SAI afferent, and as signal transformations and integration are unobservable, models are required to investigate the link between biological mechanisms and SAI afferent responses. While finite element models are able to control for skin's contribution to SAI afferent responses, understanding the contribution of the end organ has been limited to changing parameters in the scaling function [39][14]. Similarly, recent efforts to model both skin mechanics and spike initiation do not account for the branching SAI afferent end organ with its multiple sites of spike initiation.

Here, we build novel models of the SAI afferent end organ to investigate the link of receptor architecture with SAI firing properties. In an initial analysis of electrophysiological recordings, we found that the total number of Merkel cells did not correlate with firing rate, which is perplexing given that the transduction of mechanical stimuli to receptor current is believed to take place at Merkel cell-neurite complexes. *In light of this result, we combine imaging, electrophysiology, and novel computational models to test the hypothesis that variation in the end-organ structure of the SAI afferent, specifically the*

grouping of Merkel cell-neurite complexes to each spike initiation zone, accounts for differences in firing rate.

3.2 Methods

Computational Model. To test the hypothesis, we constructed computational models of the SAI afferent's end organ embedded in skin, hereafter referred to as the "end-organ model". A novel aspect of this model is the ability to represent different end-organ structures with a reconfigurable network of transduction functions, each representing a cluster of Merkel cell-neurite complexes providing receptor currents to spike initiation zones, which are in turn represented with leaky integrate and fire models. In this way, four prototypical configurations of the model were specified, each fit to electrophysiological recordings from SAI afferents. These configurations were constrained by complete 3D confocal reconstructions of SAI end organs. For example, the model configuration for a reconstructed end organ with four spike initiation zones and associated Merkel-cell groupings of 8, 5, 3, and 1, is shown in Figure 3.1A. Furthermore, individual sub-models within the reconfigurable network capture the transformation of indentation to strain energy density by skin, of strain energy density to membrane current by receptor transduction, and of current to spike times by spike initiation (Fig. 3.1B).

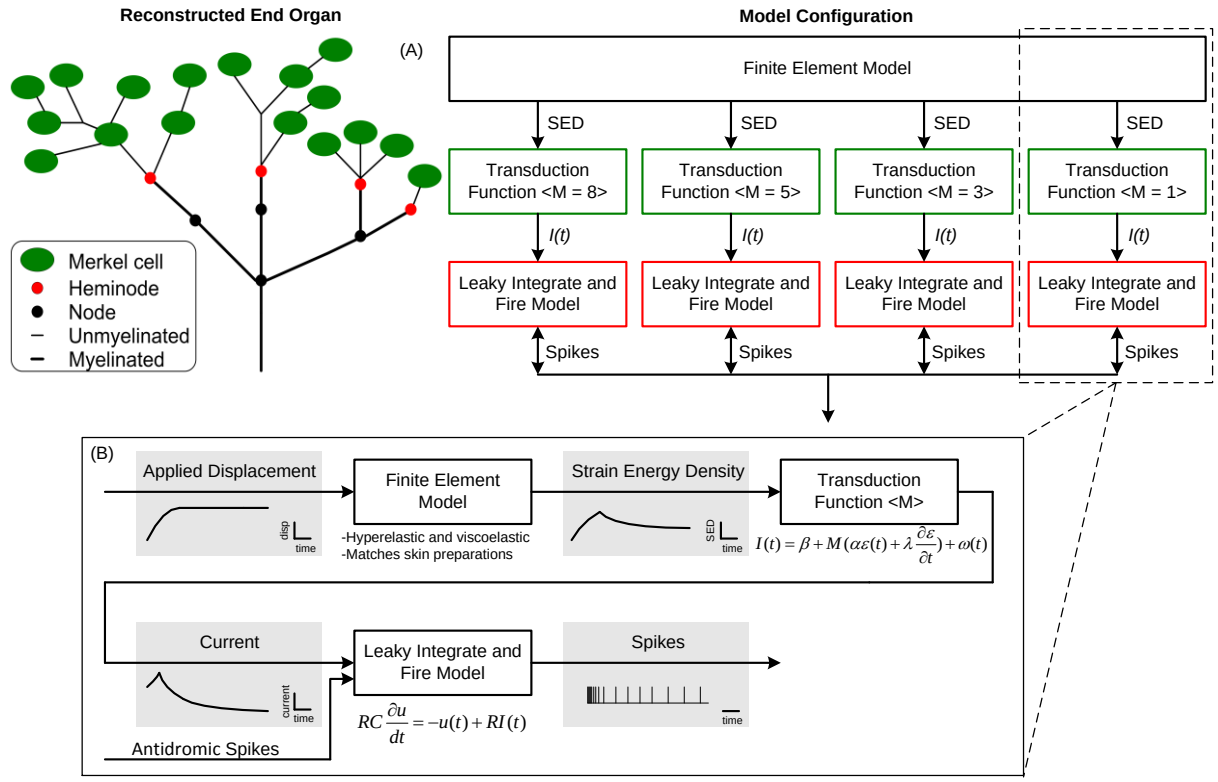

Figure 3.1: The model reconfigures to match specific SAI afferent end organs by representing the number of spike initiation zones as well as the number of Merkel cells grouped to each (A). The transformation of indentation to spike times is broken into sub-transformations completed by a finite element model of the skin, transduction functions of receptor current, and leaky integrate and fire models of neural dynamics (B). A spike generated by any leaky integrate and fire model resets and initiates refractory periods of all leaky integrate and fire models, representing the expected effect of antidromic spike propagation in the end organ.

The skin is represented with a hyperelastic (Mooney Rivlin) and viscoelastic (Prony Seies) finite element model. A two-dimensional axisymmetric mesh includes both the epidermis (17 µm thick) and dermis (224 µm thick) of the skin [35], as well as subcutaneous tissue (101 µm thick) and the elastic substrate upon which the skin rests in the experimental apparatus. Note that all skin layers and the subcutaneous tissue are modeled as having the same material properties, resulting in a homogeneous tissue layer (342 µm thick). ABAQUS Standard, version 6.6, was used to create the model's geometry and mesh, and is used for the FE analysis. The mesh utilizes four-node, bilinear quadrilateral hybrid with constant pressure elements (ABAQUS type CAX4H). The mesh contains 11200 elements. Boundary conditions are imposed such that nodes along the bottom of the substrate are constrained in the X and

Y directions. Finite element model parameters were chosen from within bounds reported for various tissues to generate displacement-force curves in close agreement with those observed in *ex-vivo* skin-nerve preparations. The resulting parameters were C10 = 14847 and C01 = 41410 for the Mooney Rivlin skin model, and E = 906098 for the linear elastic substrate. Prony parameters were $g_1 = 0.391$, $\tau_1 = 0.25$, $g_2 = 0.226$, and $\tau_2 = 9.371$. These parameters govern the model's transformation of indentation into strain energy density (SED), a measure of tissue distortion thought to correlate with the SAI afferent response [15][16][40]. SED is sampled from two elements approximating the volume and location of the SAI afferent end organ, located beneath the cylindrical probe that contacts the model's surface. This probe is specified as a rigid analytic surface with a friction coefficient of 0.3 between the probe tip and skin surfaces, and due to the large diameter of our blunt cylindrical probe (3 mm) relative to touch domes that contain the SAI afferent end organs (~0.1 mm), it is assumed that SED magnitude is uniform across Merkel cells in the end organ.

Strain energy density from the finite element model serves as input to transduction functions representing numbers of Merkel cell-neurite complexes grouped to spike initiation zones. The transduction function is defined by equation 3.1, where *I* is current, ε is SED, β is an offset, M is the number of Merkel cells in the cluster, and α and λ are gains for SED and the first derivative of SED, respectively. Each time SED is sampled and converted to current, at a frequency of 1000 Hz resulting in one sample per millisecond, the deterministic current is modified with the addition of a sample from the noise distribution, ω. This noise distribution is a 7 point moving average of Gaussian noise with a mean of zero and a standard deviation set to reproduce variable inter-spike intervals characteristic of the SAI afferent. Gaussian deviates were obtained using the Box-Muller method [41]. An initial effort with pure Gaussian noise, assumed for simplicity, was unable to reproduce the SAI afferent's characteristic ISI variability except with noise levels dominating all other current components. For this reason, time

correlations were introduced, similar to those observed in current for spinal sensory neurons [42]. Noise was added to the transduction function due to the assumption that variable inter spike intervals result from synaptic transmission from Merkel cells giving rise to noisy input to spike initiation [38]. While the modeled transduction function is linear, the true stimulus-current transformation is likely sigmoidal, as observed for nociceptors and hair cells [43][44]. While the simplifying assumption of a linear function is adequate for the stimuli used here, it would not be valid for stimuli eliciting responses approaching the SAI afferent's saturation firing rate (~1000 spikes/sec), as the model would predict firing rates higher than would be generated by the SAI afferent.

$$I(t) = \beta + M(\alpha\varepsilon(t) + \lambda\frac{\partial\varepsilon}{\partial t}) + \omega(t) \qquad \text{Eqn 3.1}$$

The current originating from the transduction functions serves as input to leaky integrate and fire models, representing spike initiation zones. Neural dynamics are abstracted to a single differential equation (Eqn 3.2), where *R* is resistance, *C* is capacitance, *u(t)* is membrane potential, and *I(t)* is current. When current drives the membrane potential to a spike initiation threshold, $\overline{v}$, a spike time is recorded and a 1 ms absolute refractory period is entered. It is expected *in vivo* that a spike generated at one spike initiation zone would antidromically invade the other spike initiation zones, resetting them and initiating an absolute refractory period [38]. Thus, when a spike is generated by a given leaky integrate and fire model, that spike resets all other leaky integrate and fire models in the modeled end organ. Numeric evaluation of the leaky integrate and fire equation is performed with the fourth order Runge-Kutta method [41].

$$RC\frac{\partial u}{dt} = -u(t) + RI(t) \qquad \text{Eqn 3.2}$$

Animal Procedures. All animal procedures for this work were conducted by Dr. Ellen Lumpkin's lab according to the National Institutes of Health *Guide for the Care and use of Laboratory Animals* and

were approved by the Department of Defense and Institutional Animal Care and Use Committees of Baylor College of Medicine and Columbia University. Two classes of data were collected: electrophysiological recordings of SAI afferent responses elicited by sustained stimuli and confocal reconstructions of SAI afferent end organs.

To constrain end-organ models, 16 representative touch domes were reconstructed. These reconstructions allowed specifying end organs as a number of spike initiation zones with a number of Merkel cells grouped to each. Based on these reconstructions, for prototypical SAI end organs were modeled: {8, 5, 3, 1}, {7, 6, 4, 2, 1}, {6, 4, 3}, and {5, 4, 3, 1}, where each number within brackets indicates the number of Merkel cells grouped to a spike initiation zone. For example, {8, 5, 3, 1} specifies four spike initiation zones, with 8, 5, 3, and 1 Merkel cells associated with each, respectively. While {8, 5, 3, 1} and {6, 4, 3} were chosen from the reconstructions, {7, 6, 4, 2, 1} and {5, 4, 3, 1} were defined to provide realistic end organ configurations representative of the range of observed variation.

End-organ models were further constrained with electrophysiological recordings from SAI afferents, which provide firing rates with which to fit the models. Single-unit responses were recorded from hairy skin dissected from the mouse hind paw with a portion of the saphenous nerve intact, as described previously [7]. These *ex-vivo* skin-nerve preparations were pinned to a 5-mm thick silicone-elastomer substrate within a two compartment organ chamber circulating synthetic interstitial fluid. After isolating a single SAI afferent, a mechanical indenter delivered controlled displacements, ranging from 0.012 to 0.362 mm with accelerations of 19.8, 81.1, and 1143.2 mm/s, to the receptive field while the elicited spikes and applied forces were recorded (Appendix A, B). Data was obtained from four female *J2x-nEGFP* mice, 13-17 weeks old and weighing 22-33 g. The firing rate in the hold phase of the stimulus was calculated by averaging the number of over a 2.5-s window starting 2 s after the probe had achieved its commanded depth. Note that the responses of these four afferents well demonstrate the

SAI afferent's characteristic variation in response for similar indentations, in terms of both absolute firing rates and sensitivities, and that responses do not correlate to total Merkel-cell number (Fig. 3.2A). For example, recordings A and D both have similar Merkel cell counts (13 and 12 Merkel cells, respectively), generate the highest and lowest firing rates for similar displacements, and are also the most and lease sensitive, respectively. Skin samples were consistent, as indicated by displacement-force relationships (Fig. 3.2B).

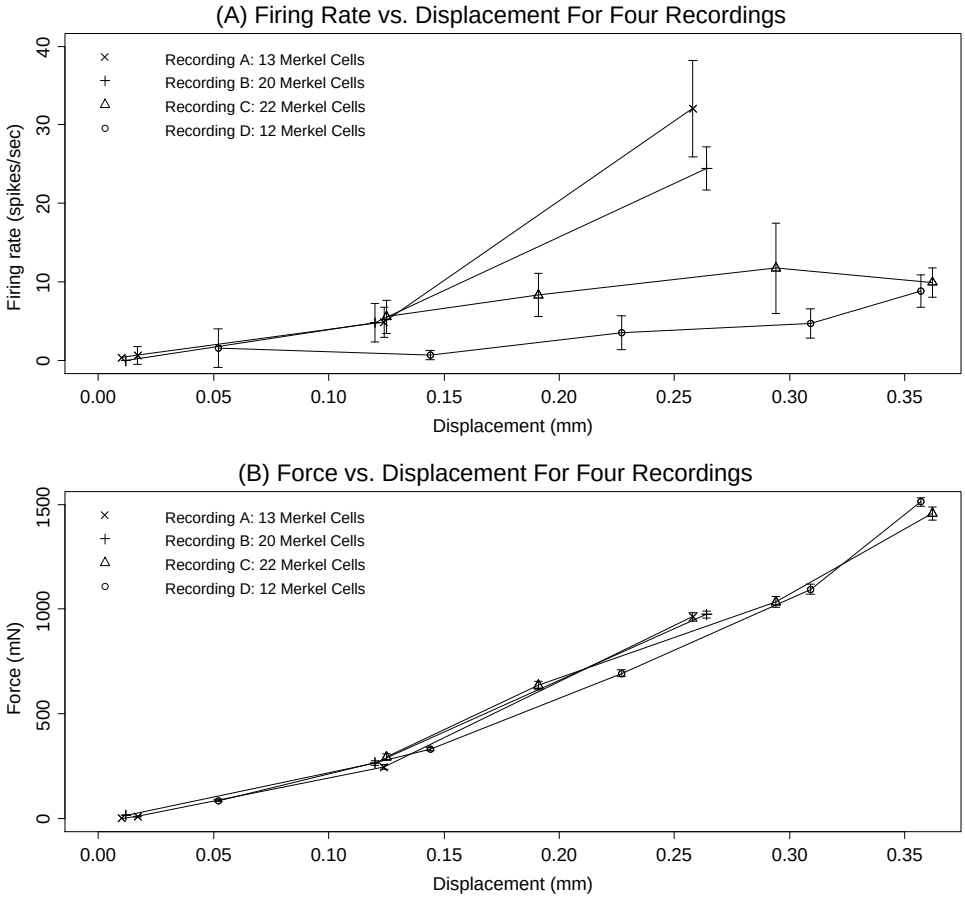

Figure 3.2: Firing rate (A) and force (B) vs. displacement for electrophysiological recordings from four SAI afferents. Note that Merkel-cell number does not correlate with sensitivity. Means±SDs are plotted. Adapted from [8].

Model Fitting. Fitting each end-organ model to the mean SAI afferent response involved three free parameters in the transduction function: β, α, and λ. These were selected with gradient free response surface methodology using Latin hyper-cube space filling designs, where each design was composed of 20 trial points (sampled using the LHS package in R). The start point was informed by a domain search utilizing 50 points in a space filling design [45]. In contrast, the skin-mechanics models were set as per the discussion above, and the leaky integrate and fire parameters were fixed at values of 5 ms, 1e^{-8} mF, and 30 mV for τ, C, and $\bar{v}$, respectively. As it is not currently possible to directly observe the electrical properties of SAI spike initiation zones, these values were assumed based on correspondence with Dr. Scott Wellnitz. Note that resting membrane potential is scaled to 0 mV, so that the 30 mV threshold represents a 30 mV change from resting.

Each of the four end-organ model configurations were fit to the mean SAI afferent responses by maximizing the combined goodness of fit, measured as fractional sum of squares, between mean and predicted firing rates. This combined goodness of fit takes a value of 2 for a model that perfectly matches the mean response profile, and is described by equation 3.3, where $\overline{hfr_i}$, hfr_i, $\overline{rfr_i}$, rfr_i are the mean experimentally observed hold phase firing rate, the predicted hold phase firing rate, the mean biological ramp phase firing rate, and the predicted ramp phase firing rate, respectively, for stimulus i. The index i spans from 1 to 75 due to 5 unique displacement depths and 3 accelerations giving 15 unique stimulations, each of which was simulated 5 times for a given set of model parameters.

$$fss_{combined} = \left(1 - \frac{\sum_{i=1}^{75}\left(\overline{hfr_i} - hfr_i\right)^2}{\sum_{i=1}^{75}\left(\overline{hfr_i}\right)^2}\right) + \left(1 - \frac{\sum_{i=1}^{75}\left(\overline{rfr_i} - rfr_i\right)^2}{\sum_{i=1}^{75}\left(\overline{rfr_i}\right)^2}\right) \qquad \text{Eqn 3.3}$$

After fitting, parameters took values shown in table 3.1 for each model configuration. These values were used for the first two computational experiments, where results were generated for each

prototypical end organ. In contrast, model parameters for the two end organ configurations in the third computational experiment (Merkel-cell grouping obscuring Merkel-cell number) were set as the parameter averages of β = 5.658 x10^{-8} mA, α = 2.545 x10^{-14} mA/Pa, and λ = 5.882 x10^{-11} mA·ms/Pa. For additional details and intermediate results, see Appendix C.

Table 3.1: Transduction parameters for four model configurations.

Configuration	β (mA)	α (mA/Pa)	λ (mA·ms/Pa)
{8, 5, 3, 1}	5.643x10^{-8}	2.539x10^{-14}	5.833x10^{-11}
{7, 6, 4, 2, 1}	5.648x10^{-8}	2.386x10^{-14}	4.994x10^{-11}
{6, 4, 3}	5.669x10^{-8}	2.612x10^{-14}	6.211x10^{-11}
{5, 4, 3, 1}	5.672x10^{-8}	2.641x10^{-14}	6.491x10^{-11}

After model fitting, three experiments were conducted to test the hypothesis that variation in the grouping of Merkel cells to each spike initiation zone accounts for differences in firing rates between SAI afferents.

Grouping of Merkel cells to spike initiation zones. To examine how variation in the grouping of Merkel cells to spike initiation zones could explain differences in SAI afferent responses, predictions from the four end-organ models were examined as their Merkel-cell grouping to spike initiation zones was varied. Specifically, changes to firing rates were observed while the largest (primary) and second largest (secondary) cluster of Merkel cells were systematically varied such that alternate groupings of Merkel cells to spike initiation zones (i) keep Merkel-cell number and spike initiation zones constant for each comparison, (ii) hold secondary cluster constant when changes to primary cluster are examined and vice-versa, and (iii) have identical changes to primary and secondary cluster sizes within a starting configuration. To examine the impact of the primary and secondary clusters, respectively, for the {8, 5, 3, 1} end organ model, comparisons were made of {10, 5, 1, 1} vs. {6, 5, 3, 3} and of {8, 7, 1, 1} vs. {8, 3, 3, 3}. Similarly, to examine the impact of the primary and secondary clusters for the {7, 6, 4, 2, 1}

end organ model, comparisons were made of {9, 6, 3, 1, 1} vs. {6, 6, 4, 2, 2} and of {7, 7, 4, 1, 1} vs. {7, 4, 4, 3, 2}. For the {6, 4, 3} end organ model, comparisons of {7, 4, 2} vs. {5, 4, 4} and of {6, 6, 1} vs. {6, 4, 3} were made. Finally, for the {5, 4, 3, 1} end organ model, comparisons of {6, 4, 2, 1} vs. {4, 4, 3, 2} and of {5, 5, 2, 1} vs. {5, 3, 3, 2} were made.

These comparisons evaluated the change in firing rate as a percentage, calculated by dividing the difference in summed firing rates between the two configurations by the lowest summed firing rate of the two. This is described by equation 3.4, where fr_{ai} and fr_{bi} are firing rates generated by the two configurations for stimulation i. The index i spans from 1 to 75 due to 5 unique displacement depths at 3 accelerations giving 15 unique stimulations, each of which was simulated 5 times. This provides a metric for comparing the overall response magnitudes of different configurations. However, averaging across different stimulus parameters obscures details of the stimulus-response transformation. For this reason, supra-threshold sensitivity was also examined, defined as the slope of a line fit through the firing rates generated by the three greatest displacements, as these points were unambiguously supra-threshold.

$$\%fr\ change = \frac{\sum_{i=1}^{75} fr_{ai} - \sum_{i=1}^{75} fr_{bi}}{\sum_{i=1}^{75} fr_{bi}}, \quad where \sum_{i=1}^{75} fr_{ai} > \sum_{i=1}^{75} fr_{bi} \qquad \text{Eqn 3.4}$$

Interaction of Merkel-cell grouping and number. A second computational experiment was run where the number of Merkel cells in four representative end organs was increased from the original number. This was done to examine the impact of Merkel-cell number, and to determine whether this impact might be obscured by the effect of Merkel-cell grouping. For each Merkel-cell increase simulated for the four prototypical end organs, two groupings of Merkel cells to spike initiation zones were used where cluster sizes were limited to the size of the largest cluster: a Merkel-cell grouping that increased

the second largest cluster first and a Merkel-cell grouping that increased the smallest cluster first. Taking the starting end organ of {8, 5, 3, 1} for example, the second largest first end organ for 18 Merkel cells is {8, 6, 3, 1} while the smallest first end organ is {8, 5, 3, 2}.

Merkel-cell grouping obscuring Merkel-cell number. A third computational experiment examined how an SAI afferent with fewer Merkel cells produce a greater firing rate than one with more Merkel cells. To allow the size of the primary cluster to vary independent of Merkel-cell number, the number of spike initiation zones was allowed to vary. Models of two end organ configurations were instantiated. The first model {10, 1, 1} had 12 Merkel cells, 3 spike initiation zones, with the largest cluster being size 10. The second model {4, 4, 4, 4, 4} had 20 Merkel cells, 5 spike initiation zones, with the largest cluster being size 4. These were chosen such that Merkel cell count and the size of the largest cluster would have opposite effects on the predicted response. Although the number of Merkel cells, size of the largest cluster, and number of spike initiation zones for these two configurations falls within the ranges observed though reconstructions, these specific groupings were not observed experimentally.

3.3 Results

Grouping of Merkel cells to spike initiation zones. The results of these comparisons (table 3.2) indicate that when the number of Merkel cells is held constant, firing rates increase with the size of the largest Merkel-cell cluster (white row for each Merkel-cell number), and to a lesser degree, with the size of the second largest Merkel-cell cluster (grey shaded row for each Merkel-cell number). On average, firing rates increased with the size of the largest Merkel-cell cluster 7.2 % per Merkel cell, and with the size of the second largest Merkel cell cluster 2.8 % per Merkel cell. These changes in firing rate appear to

increase with displacement depth, indicating corresponding changes in sensitivity (table 3.3), as shown for varying the primary (Fig 3.3A) and secondary (Fig 3.3B) cluster of the {8, 5, 3, 1} base configuration.

Table 3.2: Changes in firing rate as the largest (white rows) and second largest (colored rows) clusters of Merkel cells are varied, while keeping the total number of Merkel cells constant.

Grouping	MC number	ΔLargest	ΔSecond largest	% Firing Rate Change
{10, 5, 1, 1}	17	4	0	39%
{6, 5, 3, 3}				
{8, 7, 1, 1}	17	0	4	15%
{8, 3, 3, 3}				
{9, 6, 3, 1, 1}	20	3	0	18%
{6, 6, 4, 2, 2}				
{7, 7, 4, 1, 1}	20	0	3	9%
{7, 4, 4, 3, 2}				
{7, 4, 2}	13(a)	2	0	14%
{5, 4, 4}				
{6, 6, 1}	13(a)	0	2	5%
{6, 4, 3}				
{6, 4, 2, 1}	13(b)	2	0	12%
{4, 4, 3, 2}				
{5, 5, 2, 1}	13(b)	0	2	4%
{5, 3, 3, 2}				

Table 3.3: Changes in sensitivity as the largest (white rows) and second largest (colored rows) clusters of Merkel cells are varied, while keeping the total number of Merkel cells constant.

Grouping	Sensitivity (Spikes/sec/mm)	Change In Sensitivity (Spikes/sec/mm)
{10, 5, 1, 1}	113.00	40.0
{6, 5, 3, 3}	72.97	
{8, 7, 1, 1}	98.81	13.4
{8, 3, 3, 3}	85.37	
{9, 6, 3, 1, 1}	95.28	25.0
{6, 6, 4, 2, 2}	70.26	
{7, 7, 4, 1, 1}	83.08	20.0
{7, 4, 4, 3, 2}	63.10	
{7, 4, 2}	81.48	13.2
{5, 4, 4}	68.26	
{6, 6, 1}	81.58	9.5
{6, 4, 3}	72.11	
{6, 4, 2, 1}	66.80	6.5
{4, 4, 3, 2}	60.35	
{5, 5, 2, 1}	68.92	10.1
{5, 3, 3, 2}	58.80	

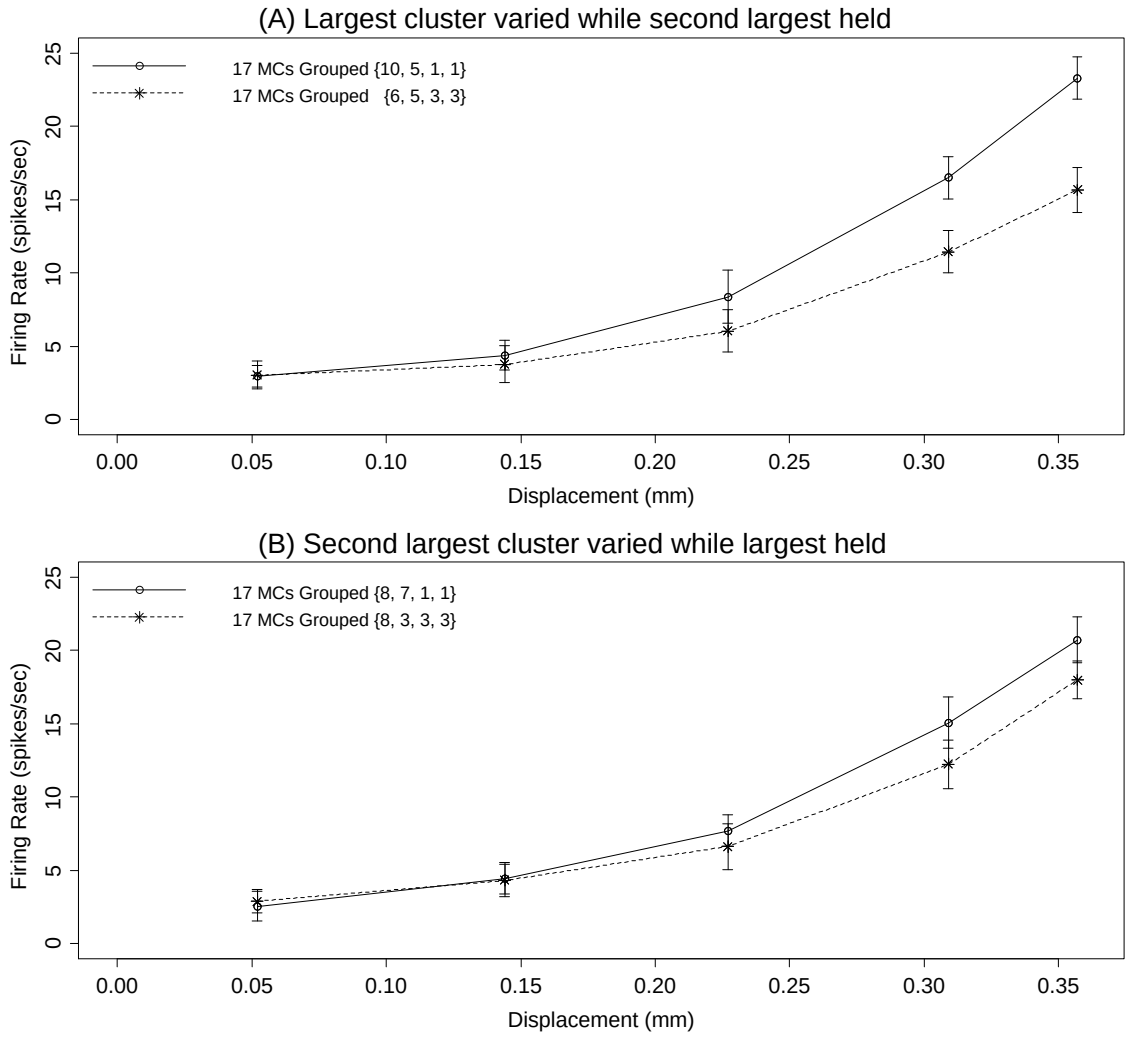

Figure 3.3: Firing rates for {8, 5, 3, 1} end-organ model while primary (A) and secondary (B) clusters are varied while holding the total Merkel-cell number at 17. Error bars denote +/- 1 standard deviation.

Interaction of Merkel-cell grouping and number. For each of the four end-organ configurations, an increase to its Merkel-cell number resulted in an increased firing rate (Fig. 3.4); however, given an increase in Merkel-cells, Merkel-cell groupings with larger cluster sizes resulted in higher firing rates than the Merkel-cell groupings with smaller cluster sizes. For example, with a base configuration of {8, 5, 3, 1} (Fig 3.4A), increasing the Merkel-cell number from 17 to 24 produces a 39% firing rate increase for a Merkel-cell grouping of {8, 8, 7, 1} and a 21% firing rate increase for a Merkel-cell grouping of {8, 6, 5, 5}. Furthermore, the impact of Merkel-cell grouping in a cluster appears to obscure the

impact of Merkel-cell increase in some cases. For example, with a base configuration of {8, 5, 3, 1} (Fig 3.4A), increasing the Merkel-cell number from 17 to 20 with a grouping of Merkel cells to spike initiation zones of {8, 8, 3, 1}, produced similar increase in firing rate as a Merkel-cell increase from 17 to 24 with a grouping of Merkel cells to spike initiation zones of {8, 6, 5, 5}.

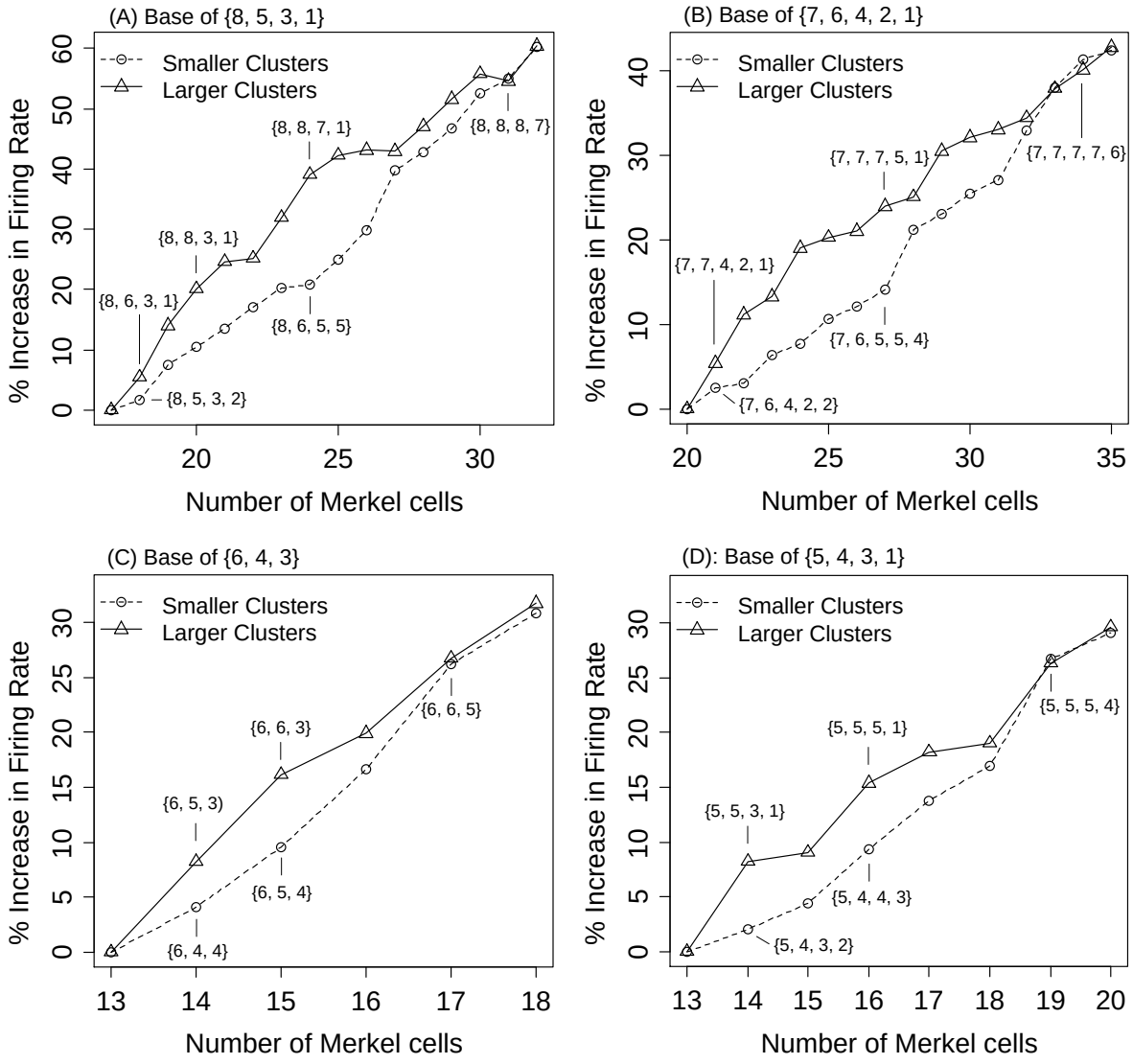

Figure 3.4: Changes in firing rate as Merkel-cell number is increased for each of the four end-organ model configurations of {8, 5, 3, 1} (A), {7, 6, 4, 2, 1} (B), {6, 4, 3} (C), and {5, 4, 3, 1} (D). Each Merkel-cell increase is performed under two policies: increasing the second largest cluster first, causing larger clusters (solid line, triangle markers), and increasing the smallest cluster first, causing smaller clusters on average (dashed line, circle markers). Percent firing rate increases are in comparison to the base configurations.

Merkel-cell grouping obscuring Merkel-cell number. The configuration {10, 1, 1} generated higher firing rates at the upper end of the displacement range, despite having eight fewer Merkel cells than the {4, 4, 4, 4, 4} configuration (Fig. 3.5). Although firing rates appear slightly higher for the {4, 4, 4, 4, 4} configuration for the lower displacements (p=0.002), resulting in roughly 3 more spikes over the static hold, overall the {10, 1, 1} configuration corresponds to a 10% firing rate increase. Note the increased sensitivity of 119.0 spikes/s/mm for the {10, 1, 1} afferent, as compared to 68.8 spikes/s/mm for the {4, 4, 4, 4, 4} afferent, a difference of 50.2 spikes/s/mm.

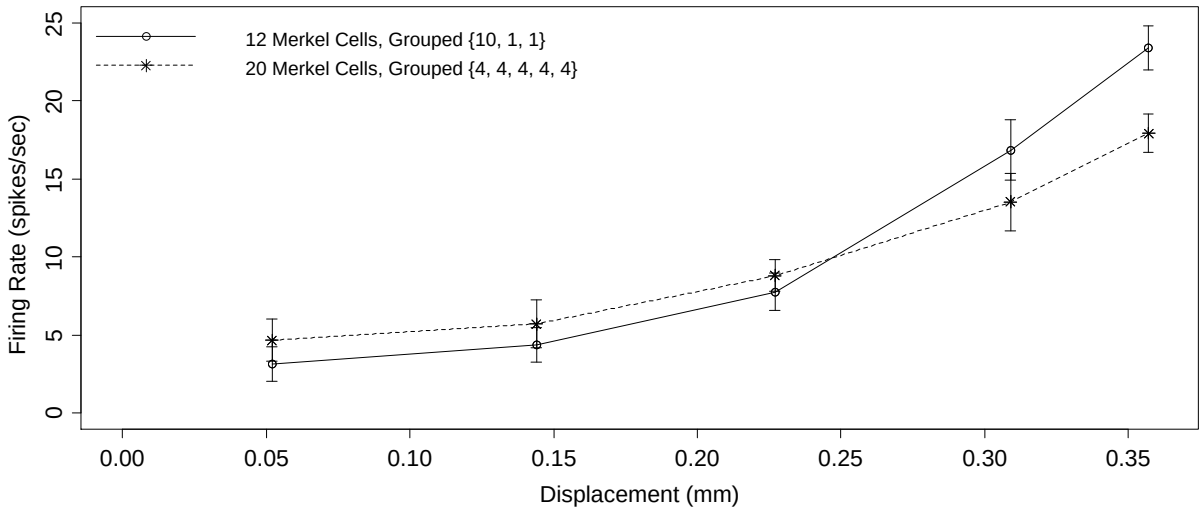

Figure 3.5: Firing rates for configurations of {10, 1, 1} and {4, 4, 4, 4, 4}. Error bars denote +/- 1 std.

3.4 Discussion

The work in Aim 1 develops a computational model of the end organ of the SAI afferent embedded in skin, informed by confocal imaging and electrophysiology. To the best of our knowledge, this represents the first effort to account for multiple spike initiation zones, associations of spike initiation zones with clusters of Merkel cells, and variations in the number of Merkel cells. This work was motivated, in part, by our observation that the sensitivity of the SAI afferent did not correlate with Merkel-cell number in our electrophysiological recordings. For example, recordings A and D in figure 3

have similar Merkel-cell counts, 13 and 12 respectively, but are the most and least responsive of the four recordings, respectively. Furthermore, if one were to observe only recordings A, B, and C, he or she might be lead to believe that responsiveness is inversely related to Merkel-cell number. This is perplexing given that the transduction of mechanical distortion to receptor current is believed to take place at Merkel cell-neurite complexes, though at the Merkel cell or neurite is unresolved [36]. The simulation results presented here may explain this paradox by demonstrating that although Merkel-cell number does impact SAI afferent sensitivity, a second factor that can neither be observed nor controlled in electrophysiological recordings obscures this relationship. This second factor is the grouping of Merkel cells to spike initiation zones. In particular, the size of the largest cluster of Merkel cells seems to have a large impact on the response. For example, a model configured with 17 Merkel cells and a Merkel-cell grouping of {10, 5, 1, 1} generates 39% higher firing rates that a model configured with 17 Merkel cells and a Merkel-cell grouping of {6, 5, 3, 3}. This demonstrates how end organs with the same number of Merkel cells can exhibit quite different responses. Furthermore, a model configured with 12 Merkel cells and a Merkel-cell grouping of {10, 1, 1} generates 10% higher firing rates and is 50.2 spikes/s/mm more sensitive than a model configured with 20 Merkel cells and a Merkel-cell grouping of {4, 4, 4, 4, 4}, demonstrating how end organs with more Merkel cells may be less sensitive than end organs with fewer.

Consequentially, this work suggests that the most sensitive SAI afferent would cluster all Merkel cells to a single spike initiation zone, or, given a number of spike initiation zones, have a skewed distribution where all but one was associated with a single Merkel cell. Interestingly, this is not the case *in vivo*. In a survey of 16 SAI afferent end organs, which were reconstructed with whole-mount immunostaining, all had three to five spike initiation zones with asymmetric clusters [8]. It is possible that SAI afferents innervate multiple Merkel cells for increased robustness to injury, in addition to

increased sensitivity [46], and that the grouping of Merkel cells to spike initiation zones mediates a tradeoff between these two competing factors. It is also possible that asymmetric clusters could extend the SAI afferent's range of sensory coding [47].

It should be noted that the model abstracts the neurite length between Merkel cells and spike initiation zones. However, based on an observed average neurite diameter of 1 μm and a specific resistance of 25500 $\Omega \cdot cm^2$, representing a midpoint between a range in other neurons [48], the neurite length constant would be around 714 μm, an order of magnitude greater than the mean path length 35.26 μm, SD=10.93 μm (N=12, taken from {8, 5, 3, 1} reconstruction). Similarly, the model assumes equivalent Merkel cell-neurite complexes. However, transduction units tuned to different stimulus features may underlie the encoding of both dynamic and static stimuli, as proposed for muscle-spindle afferents [49][50].

This joint modeling and experimental effort fits within the emerging paradigm of using computational methods to gain insight into perceptual mechanisms not amenable to direct observation. For example, mechanics modeling has investigated the link of experimentally unobservable mechanical states within the skin of primates [39][16] or the tactile hairs of spiders [51] and neural responses. Similar methods have been used to investigate the role of end organ morphology for the Pacinian corpuscle, and demonstrate that the external shape of the corpuscle is likely irrelevant to the neural response, suggesting that the internal layered structure of the corpuscle is of primary importance [52]. While these investigations have primarily been mechanical in nature, others have attempted to link end-organ mechanics with spike initiation to create a more unified understanding of tactile sensation [53]. The work presented here complements these efforts by also considering internal electrical structure, which is of particular importance for the SAI afferent's branched end organ.

Finally, ever since touch domes were identified as a source of slowly adapting responses that contain innervated Merkel cells, understanding the role of Merkel cells in the SAI afferent response has been a central question [2]. Recently, Merkel cell-neurite complexes were definitively confirmed as the source of SAI afferent responses through a combination of *ex-vivo* recording, neuronal tracing, and post hoc histological analysis [3]. Furthermore, *Atoh1* knockout mice, devoid of Merkel cells, have been shown to lack SAI afferent responses through *ex-vivo* recordings [54]. The work described here complements these efforts, which demonstrate that Merkel cells are essential to SAI afferent responses, by beginning to explore how the complement of Merkel cell-neurite complexes mediate the input-output relationship of the SAI afferent.

3.5 Acknowledgments.

This work would not be possible without the contributions of colleagues in Dr. Ellen Lumpkin's lab. In particular, end organ reconstructions were performed by Kara Marshall and electrophysiology was performed by Dr. Scott Wellnitz. The computerized indenter for electrophysiology was characterized with laser tracking experiments performed by Dr. Yoshichika Baba (appendix A). Similarly, this work would not be possible without finite element modeling assistance from William Carson in Dr. Gregory Gerling's lab. Furthermore, this work was greatly improved through discussion with Dr. Gregory Gerling, Yuxiang Wang, Dr. Ellen Lumpkin, Kara Marshall, Dr. Scott Wellnitz, and Dr. Yoshichika Baba.

4. Changes to SAI Afferent Responses due to End Organ Remodeling may be Mitigated by Skin Thickness Changes During the Mouse Hair Cycle

Immunostaining experiments have recently shown that the number of Merkel cells in an end organ increases by roughly 42% over a period of weeks with the hair cycle (Unpublished, Marshall and Lumpkin)[55]*. Here, we seek to understand the impact of such a change on the SAI afferent response, and determine if the expected impact could be counteracted by a simultaneous change in skin thickness, which varies from 147 to 433* μm *over the same time frame. To do so, we utilize computational models of the SAI end organ composed of transduction functions representing groups of Merkel cells and leaky integrate and fire models representing spike initiation zones, combined with multiple finite element models, each of which reflects a different skin thickness within an experimentally observed range. Simulation results indicate that while the increasing number of Merkel cells causes an increase in firing rate, a simultaneous increase in skin thickness causes a counteracting decrease. For example, if a change in skin thickness is not accounted for, end organ remodeling resulted in an average firing rate increase of 37% and a supra-threshold sensitivity change of 32.2 spikes/sec/ms, compared to an average of just 1% and 1.3 spikes/sec/ms when a change in skin thickness is modeled. Therefore, this work indicates that simultaneous variation in the SAI afferent end organ and the skin in which it is embedded may maintain homeostasis with respect to SAI afferent responses.*

4.1 Introduction

Little is known about how the stimulus-response transformation of individual SAI afferents may vary with time, although biological mechanisms underlying touch sensation, such as the SAI afferent end organ and skin, change over time. For example, during the hair cycle, where hair follicles grow (anagen), regress (catagen), and enter a state of quiescence (telogen) over a period of weeks [56], both the end organ and skin change [55][56][57]. While this process is mosaic in humans, the synchronized hair cycles in mice provide an experimentally tractable model for examining how the end organ and skin may interact over time. In mice, skin thickness changes such that during active stages (anagen + catagen) it is significantly thicker than during rest stages (telogen) [56][57]. Similarly, immunostaining reconstruction experiments have recently shown that the SAI end organ appears to structurally remodel between rest and active stages of the hair cycle such that the number of Merkel cells increases by 42%, while the number of spike initiation zones remains unchanged *(Unpublished, Marshall and Lumpkin)*[55]. Given that Merkel cell configuration is tied with the neural response, this paradoxically suggests that the input-output relationship of the SAI afferent, in terms of both response magnitude and supra-threshold sensitivity, may vary with the hair cycle.

Currently, it is not possible to record from an individual SAI afferent over a period of weeks, nor have skin thickness measurements and end-organ reconstructions been obtained from the same skin-nerve preparation. However, computational modeling may facilitate our understanding of how changes to the skin and end organ impact the SAI afferent response over time. Previous modeling efforts have either focused on how skin mechanics and structure shape the neural response [13][16][40] or on how the structure of the SAI end organ influences afferent-to-afferent variability [8]. *Here, we combine computational models of the SAI end organ with recent measurements of skin thickness to test the*

hypothesis that the thickening of the skin between rest and active stages mitigates the impact on neural firing that might be induced by remodeling of the end organ, thereby promoting homeostasis.

4.2 Methods

To test this hypothesis, we model SAI end-organs as a reconfigurable network of transduction functions and leaky integrate and fire models, and model the skin with multiple finite element models, each of which represents a different thickness covering the observed range for rest (9.0 - 11.1 weeks of age) and active (5.7 – 6.9 weeks of age) stages over a hair cycle. Using these tools, three computational experiments are run to 1) examine how the range of skin thicknesses impacts the SAI response, 2) test whether the expected change in firing properties between rest and active stage end organs might be counteracted by a concurrent thickening of the skin, and 3) examine the expected mitigation of end-organ remodeling should skin change between median thickness values for rest and active stages rather than values dependent on the end organ.

The first computational experiment examines the feasibility that between rest and active stages, increasing skin thickness impacts firing rate. To do so, four prototypical rest stage end-organ models were run with six finite element models of differing skin thickness. Skin thickness from 147 to 433 μm were simulated with 57 μm increment changes to thickness. This range was experimentally observed for rest and active stages over a period of five weeks [57].

The second computational experiment tested whether increasing skin thickness can counteract the impact of increased Merkel cell count in active stage end organs. Comparisons were first made between firing rates for the four rest stage end-organ models and 3 randomly generated active stage end organs for each, all using the same finite element model. This provided an indication of the degree to which firing rate may change due to end organ remodeling, ignoring the impact of skin. Second, the

active stage end organ models were run with skin thicknesses within the range examined in the first computational experiment, where thicknesses were selected to reduce the percent change in firing rate to within 5% without overcorrecting. Note that in addition to the finite element models in the first computational experiment, finite element models of 404 μm and 347 thick skin were also used to provide intermediate values when the adjacent thickness values either over or under compensated.

The third computational experiment examines the effect of skin changing between median values for rest and active stages, i.e. as expected should skin change independently, in contrast to the previous experiment where skin changed dependent on the end organ. Two finite element models are utilized, reflecting the median values for rest (225 μm) and active stages (331 μm)[57]. Rest and active stage end organs are then simulated with these skin thicknesses.

In each of the three computational experiments, different skin thicknesses are reflected through the use of multiple finite element meshes. Overall, ten finite element models were variously employed over the three computational studies, as described in table 4.1. Each finite element model represents skin (with all tissue layers combined) with hyperelastic (Mooney Rivlin) and viscoelastic (Prony Seies) material models analyzed with ABAQUS Standard, version 6.6. Based on previous work [8], parameters were C10 = 14847 and C01 = 41410 for the Mooney Rivlin skin model, E = 906098 for the linear elastic substrate, and $g_1 = 0.391$, $\tau_1 = 0.25$, $g_2 = 0.226$, and $\tau_2 = 9.371$ for the Prony series. Each two-dimensional axisymmetric mesh contains 11200 four-node, bilinear quadrilateral hybrid with constant pressure elements (ABAQUS type CAX4H). Meshing was performed such that element sizes in the sampling region were identical between meshes, and boundary conditions are imposed such that nodes along the bottom of the substrate are constrained in the X and Y directions. A friction coefficient of 0.3 between the rigid analytic probe and skin surfaces was specified.

Table 4.1: Summary of 10 meshes used, including skin thickness reflected and which computational experiments it contributed to

FEM	Skin Thickness (μm)	Utilized in Experiment(s)
1	147	1, 2
2	204	1
3	261	1
4	318	1, 2
5	375	1, 2
6	433	1, 2
7	404	2
8	347	2
9	225	3
10	331	3

Four rest-stage end organs with Merkel cell groupings of {11, 7, 2}, {9, 7, 3}, {7, 5, 2}, and {5, 5, 3} were chosen from immunostaining reconstructions to cover a representative range of primary cluster sizes. The number of spike initiation zones was fixed at three, as we have observed it to be the most common number. Three active stage end organs were generated for each of the four rest stage end organs by increasing the Merkel cell count 42%, as determined by comparisons of 9 rest stage and 8 active stage end organs *(Unpublished, Marshall and Lumpkin)*[55]. Merkel cells were added randomly to the three spike initiation zones with equal probability. Based on previous work [8], leaky integrate and fire parameters were τ =5 ms, C =1e^{-8} mF, and $\overline{v}$ =30 mV, and transduction parameters were β = 5.658 x10^{-8} mA, α = 2.545 x10^{-14} mA/Pa, and λ = 5.882 x10^{-11} mA·ms/Pa, for all end organ models.

Predicted firing rates were evaluated in terms of both sensitivity and response magnitude. Response magnitude was evaluated as the percentage change in firing rate, calculated by dividing the difference in summed firing rates between two cases by the base case compared to. Supra-threshold sensitivity was defined as the slope of a line fit through the firing rates generated by the three greatest displacements, as these points were unambiguously supra-threshold.

4.3 Results

The results of the first computational experiment indicate that as skin thickness increases, hold phase firing rate magnitude decreases (table 4.2), and that there is a corresponding decrease in sensitivity to supra-threshold stimuli (table 4.3). On average, firing rate decreased 30% as skin thickness increased between 147 and 433 µm. These changes were fairly linear, with each 57 µm increase in thickness resulting in a roughly 6% drop in firing rate. Over the range of skin thicknesses, supra threshold sensitivity changed, on average, 36 spikes/sec/mm. These results are illustrated in plots of predicted firing rate vs. displacement for 147 and 433 µm thick skin (fig. 4.1).

Table 4.2: Percent firing rate change as skin thickens for four prototypical rest stage end organs.

Skin Thickness	{11, 7, 2}	{9, 7, 3}	{7, 5, 2}	{5, 5, 3}
147 µm	0 %	0 %	0 %	0 %
204 µm	-8 %	-7 %	-8 %	-6 %
261 µm	-14 %	-14 %	-15 %	-13 %
318 µm	-19 %	-19 %	-21 %	-19 %
375 µm	-26 %	-24 %	-24 %	-21 %
433 µm	-30 %	-28 %	-32 %	-29 %

Table 4.3: Supra-threshold sensitivity (spikes/sec/mm) as skin thickens for four prototypical rest stage end organs

Skin Thickness	{11, 7, 2}	{9, 7, 3}	{7, 5, 2}	{5, 5, 3}
147 µm	168.2	153.7	102.6	85.9
204 µm	161.4	138.6	93.8	68.2
261 µm	151.3	131.4	89.4	67.1
318 µm	144.7	117.8	82.7	62.8
375 µm	142.1	107.8	72.6	59.0
433 µm	134.4	105.5	73.3	51.4

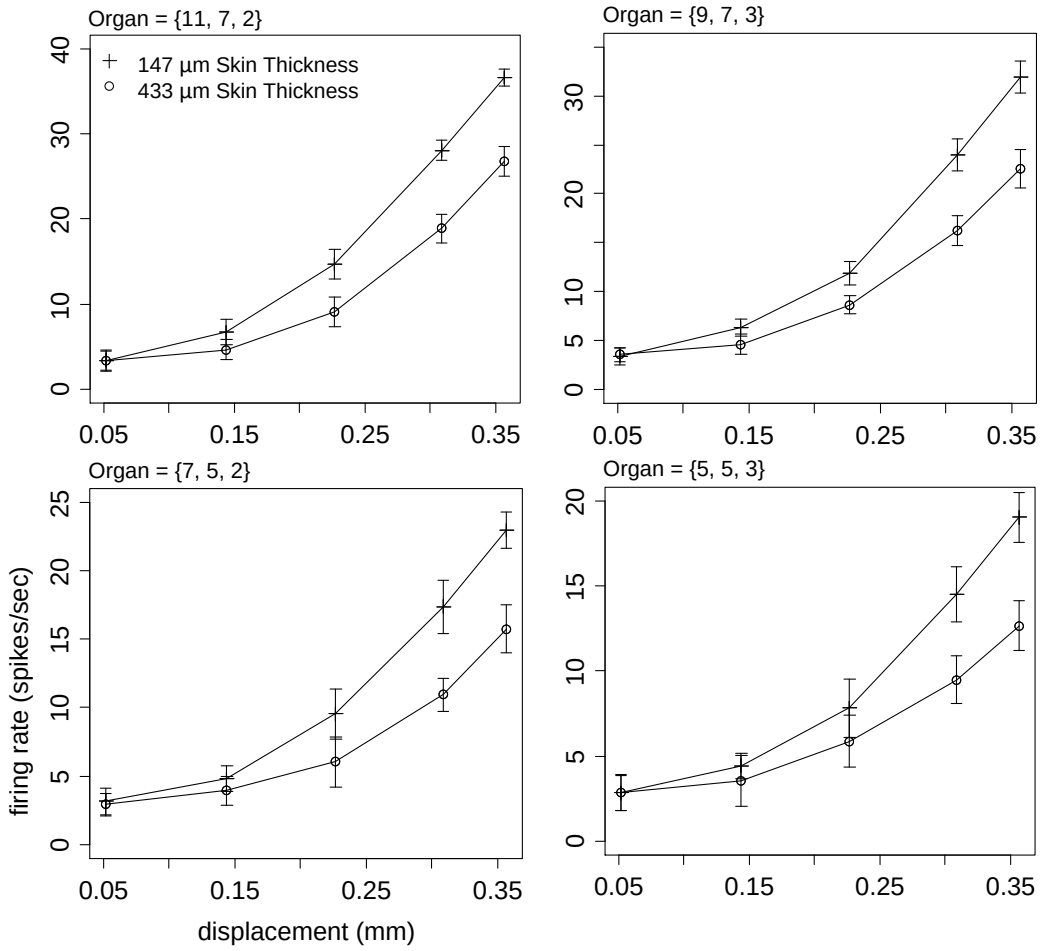

Figure 4.1: Firing rate for four prototypical rest stage end organs as skin thickness changes from 147 to 433 µm. Error bars denote +/- 1 standard deviation.

The results of the second computational experiment suggest that while the increasing number of Merkel cells causes an increase in firing rate, simultaneous increase in skin thickness causes a counteracting decrease (table 4.4), and also reduces the change in supra-threshold sensitivity (table 4.5). When the skin is held constant, changing from rest to active end organs resulted in an average firing rate increase of 37%. Conversely, when skin thickness varied with end organ, firing rate increased just 1% on average. The percent firing rate change is 36% less when the skin varies, as compared to when it remains constant. On average, supra-threshold sensitivity changed 32.2 spikes/sec/ms when the

skin remained constant, as compared to an average of 1.3 spikes/sec/ms when the skin varies. Note that firing rates when the skin varies (dotted line) are in close agreement with the firing rates from rest stage end organ models (lower solid lines) (Fig 4.2). These results suggest that skin thickness and the number of Merkel cells in the SAI end organ may interact, maintaining homeostasis.

Table 4.4: Percent firing rate change as the end organ transitions from rest stage to active stage. Results are shown for **skin held constant**, and for when **skin changes**.

Rest Organ	Active Organ	Skin Constant	Skin Changes	Skin Thickness Changed to
{11, 7, 2}	{15, 10, 3}	36%	2%	404 µm
	{13, 11, 4}	29%	1%	347 µm
	{12, 12, 4}	26%	2%	318 µm
{9, 7, 3}	{13, 10, 4}	46%	2%	433 µm
	{11, 8, 8}	31%	1%	375 µm
	{10, 10, 7}	29%	0%	375 µm
{7, 5, 2}	{10, 7, 3}	45%	1%	433 µm
	{9, 7, 4}	35%	0%	375 µm
	{9, 6, 5}	34%	1%	375 µm
{5, 5, 3}	{8, 6, 4}	49%	0%	433 µm
	{7, 7, 4}	45%	1%	404 µm
	{7, 6, 5}	38%	1%	404 µm

Table 4.5: Change in supra-threshold sensitivity (spikes/sec/mm) as the end organ transitions from rest stage to active stage. Results are shown for **skin held constant**, and for when **skin changes**.

Rest Organ	Active Organ	Skin Constant	Skin Changes	Skin Thickness Changed to
{11, 7, 2}	{15, 10, 3}	35.2	-0.6	404 µm
	{13, 11, 4}	17.2	-10.0	347 µm
	{12, 12, 4}	18.1	1.1	318 µm
{9, 7, 3}	{13, 10, 4}	45.6	9.7	433 µm
	{11, 8, 8}	29.1	-4.2	375 µm
	{10, 10, 7}	29.8	7.8	375 µm
{7, 5, 2}	{10, 7, 3}	44.1	-2.2	433 µm
	{9, 7, 4}	27.7	-6.0	375 µm
	{9, 6, 5}	29.4	2.8	375 µm
{5, 5, 3}	{8, 6, 4}	35.9	7.2	433 µm
	{7, 7, 4}	41.1	-1.3	404 µm
	{7, 6, 5}	33.4	11.2	404 µm

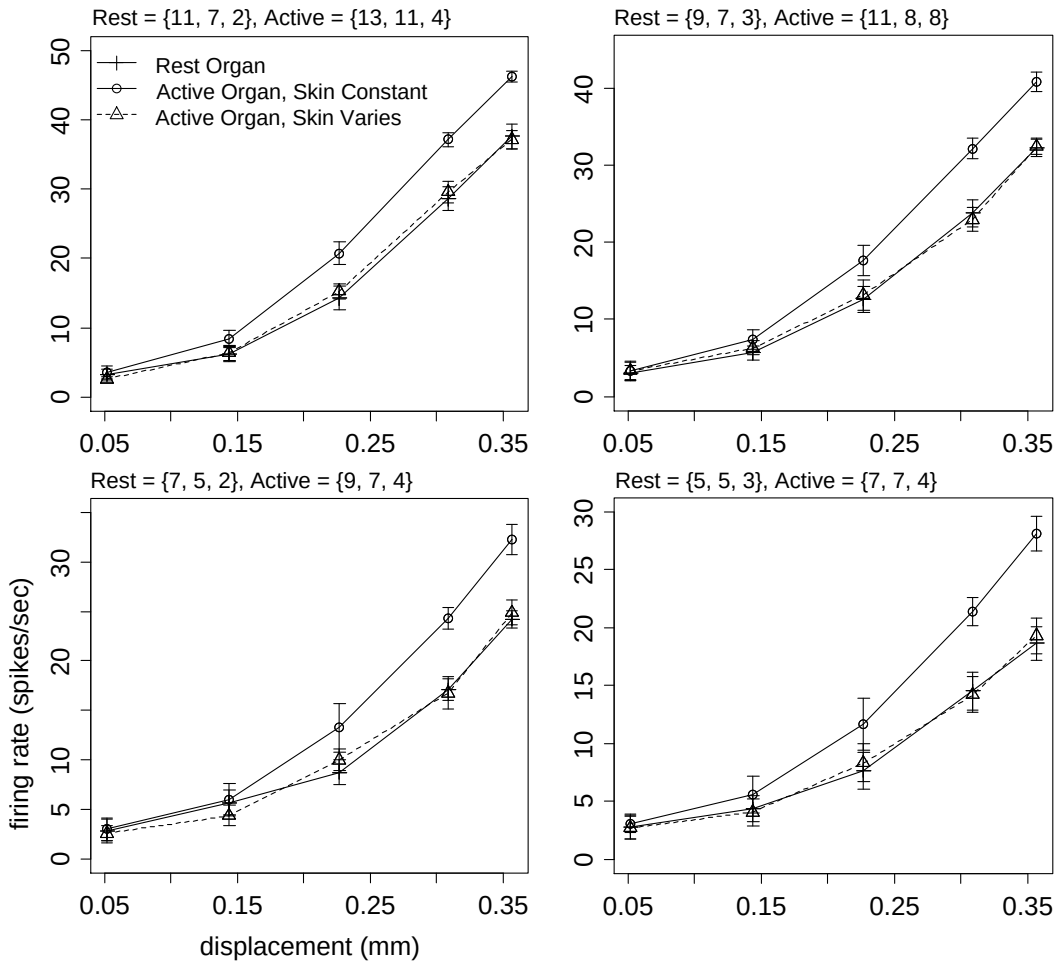

Figure 4.2: Firing rate vs. displacement for rest stage organs, active stage organs with skin thickness held constant, and active stage organs with skin that varies to mitigate the increased firing rate due to end-organ changes. Error bars denote +/- 1 standard deviation.

The results of the third computational experiment indicate that even if the skin varies independent of the end organ, it does mitigate the change in firing rate as the end organ remodels. This can be seen for both response magnitude (table 4.6) and supra-threshold sensitivity (table 4.7). When the end organs transition between rest and active stages, the firing rate changes an average of 34% if the skin does not change, compared to an average of 18% when it does. On average, supra-threshold sensitivity changed 38.6 spikes/sec/ms when the skin remained constant, as compared to an average of 21.6 spikes/sec/ms when the skin changed. Graphically, the displacement-firing rate curves for active

stage organ models using the active stage FEM fall between the simulated rest stage, and the simulated active stage end organ for when skin is constant and has no impact (fig 4.3).

Table 4.6: Percent firing rate change as the end organ transitions from rest stage to active stage. Results are shown for **skin held constant** at median thickness for rest stage, and for when **skin changes** to median thickness for active stage.

End-Organ Change	Skin Constant	Skin Changes
{11, 7, 2} -> {13, 11, 4}	29%	16%
{9, 7, 3} -> {11, 8, 8}	28%	15%
{7, 5, 2} -> {9, 7, 4}	38%	19%
{5, 5, 3} -> {7, 7, 4}	42%	20%

Table 4.7: Change in supra-threshold sensitivity (spikes/sec/mm) as the end organ transitions from rest stage to active stage. Results are shown for **skin held constant** at median thickness for rest stage, and for when **skin changes** to median thickness for active stage.

End-Organ Change	Skin Constant	Skin Changes
{11, 7, 2} -> {13, 11, 4}	33.9	13.5
{9, 7, 3} -> {11, 8, 8}	34.3	21.4
{7, 5, 2} -> {9, 7, 4}	43.3	28.6
{5, 5, 3} -> {7, 7, 4}	42.7	22.9

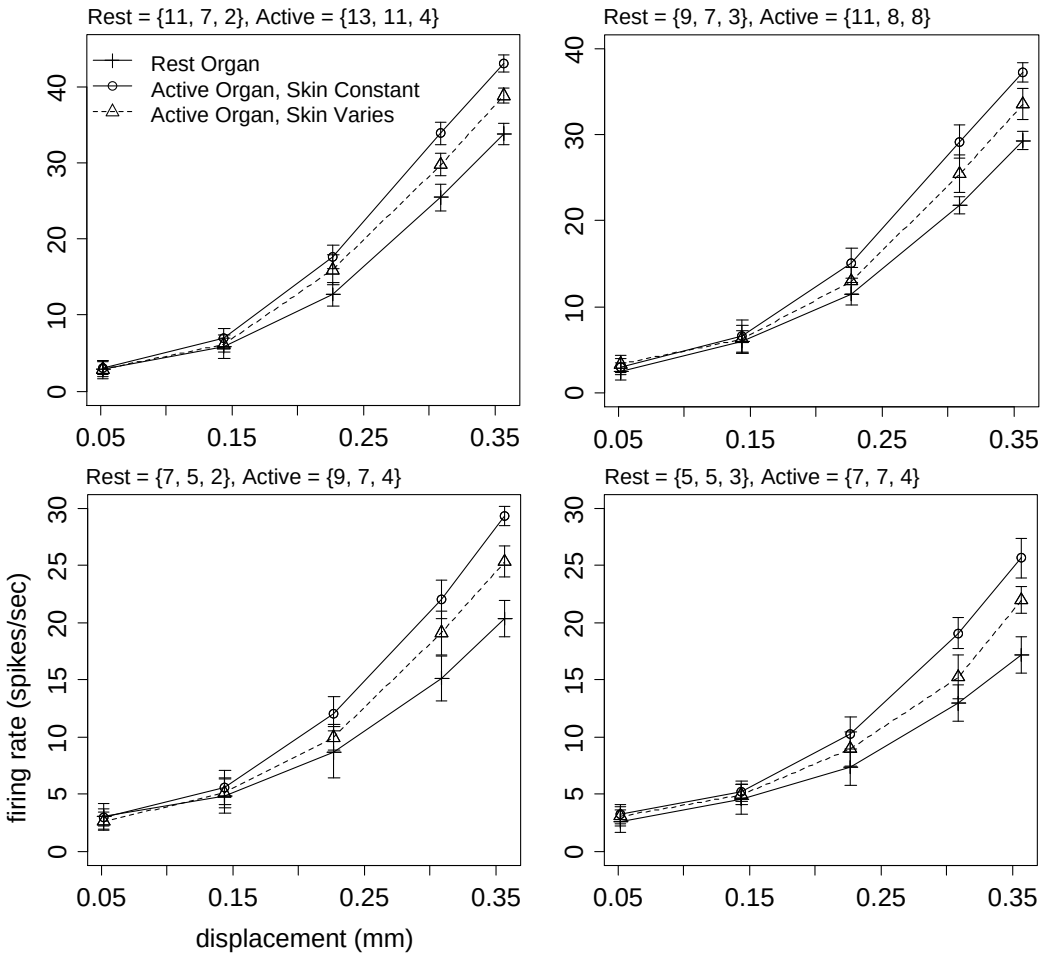

Figure 4.3: Firing rate vs. displacement for rest stage organs, active stage organs with skin held constant, and active stage organs with skin that varies to the median active stage value. Error bars denote +/- 1 standard deviation.

4.4 Discussion

This work combines computational models of the SAI end organ and multiple finite element models, each representing a different skin thickness, constrained by reconstructions of SAI end organs and skin thickness measurements. To the best of our knowledge, this is the first effort to simultaneously consider the impact of skin and end organ, as well as the first effort to consider changes to individual SAI afferent stimulus-response transformations over time. This was motivated by the observation that SAI

end organs remodel with the hair cycle such that there is a 42 percent increase in Merkel cells in the active stage as compared to the rest stage, and by the fact that our previous modeling efforts suggest such changes would significantly alter the SAI afferent's stimulus-response transformation.

The simulation results presented here demonstrate that while the increasing number of Merkel cells in active-stage end organs causes an increase in firing rate, a simultaneous increase in skin thickness causes a corresponding decrease. For example, a simulated end organ with a Merkel cell grouping of {7, 5, 2} experiences a 32 % drop in firing rate with a corresponding 29.3 spike/sec/mm decrease in supra-threshold sensitivity when modeled skin thickness changes from 147 μm to 433 μm, comparable with the 35 % increase in firing rate when the number of Merkel cells increased 42% to a grouping of {9, 7, 4}. Even if skin thickness varies independently from the end organ (though on the same time scale), results indicate that changes in skin thickness mitigate the impact of end organ remodeling. For example, simulations indicate that as an end organ remodels from a configuration of {7, 5, 2} to {9, 7, 4}, there would be a 38% change in firing rate and a 43.3 spike/sec/mm change in supra-threshold sensitivity if the skin had no impact, compared to a 19% increase in response magnitude and a 28.6 spike/sec/mm change in supra-threshold sensitivity due to median changes in skin thickness.

It should be noted that variation between SAI afferents is, in general, greater than the variation explored here. For example, in the electrophysiological data examined previously [8], supra-threshold sensitivities ranged from 21 to 202 spikes/second/mm, and firing rates differed by 120 to 665%, as compared to the least responsive SAI afferent. In contrast, changes to supra-threshold sensitivities were on the order of tens of spikes/sec/mm, and firing rates differed by up to 49%. However, that is not to say the variation explored here is insignificant. For example, if the skin does not vary, models predict equal or higher firing rates for 0.31 mm indentations during the active stage than 0.36 mm indentations during the rest stage. While high afferent to afferent variability requires upstream mechanisms to

compensate at a population level, perhaps by differently weighting afferents, temporal variability in individual afferents suggests that either the mechanisms compensating for afferent to afferent variability themselves vary with time, or homeostasis is somehow maintained in the periphery.

For interactions between skin and the end organ to promote homeostasis, coordination is required either between the SAI end organ and the surrounding tissue, or both the skin and end organ must be influenced by common signaling pathways. Signaling appears to take place between hair follicles and their local environment during the hair cycle, as follicles synchronize in spatial domains, and can be reset by pregnancy [58]. Indeed, researchers are beginning to uncover the underlying signals regulating follicle regeneration [59]. Determining if such mechanisms mutually influence the skin and end organ is beyond the scope of this work, but these studies are suggestive that coordination between the skin, follicle, and end organ may exist.

Though the skin and end organ were examined within the context of the hair cycle, this study also provides general insight into their interaction. In general, thicker skin yields lower mechanical quantities local to the SAI end organ, resulting in lower firing rates, while increased Merkel cell counts or larger clusters result in higher firing rates. A similar effect is expected where increased skin stiffness yields higher mechanical quantities local to the SAI end organ, and therefore higher firing rates. While skin stiffness does not seem to depend on hair cycle stage [57], changes in skin stiffness have been observed over longer time periods with age [60][2]. Similarly, recent reconstructions reveal the SAI end organ's arbor simplifies with age *(Unpublished, Marshall and Lumpkin)* [55]. It is not yet known how age related changes to the end organ and skin interact.

The role of skin mechanics in the SAI afferent response has been a central question for more than 30 years. For example, Johnson demonstrated that the way in which skin focuses mechanical

stresses/strains along edges helps to embed spatial information in the SAI afferent response [33][13]. More recently, skin mechanics modelers have sought to understand the link between SAI afferent responses and nonlinear skin mechanics [18], skin macrostructure [16] , and skin microstructure [40]. The work described here complements these efforts, which demonstrate that the skin and SAI afferent are intertwined, by exploring how skin mechanics and end organ structure may interact to promote homeostasis.

4.5 Acknowledgments.

This work would not be possible without the contributions of colleagues in Dr. Ellen Lumpkin's lab. In particular, end organ reconstructions were performed by Kara Marshall. Similarly, this work would not be possible without skin measurements performed by Yuxiang Wang (Member of Dr. Gerling's Lab) with Dr. Yoshichika Baba and Kara Marshall. Yuxiang Wang also assisted with finite element modeling. Furthermore, this work was greatly improved through discussions with Dr. Gregory Gerling, Yuxiang Wang, Dr. Ellen Lumpkin, Kara Marshall and Dr. Yoshichika Baba.

5. Mimicking the SAI Afferent End Organ Increases Artificial Touch Sensor Durability

Recent interest in building sensors that mimic natural tactile afferents has led to the combination of single force transducers with computational models of neural spike generation. As an extension, such sensors might leverage the compound nature of the slowly adapting type I (SAI) afferent end organ. By mimicking its structural elements, specifically multiple sites of spike initiation that reset each other, gains in durability may be obtained. Therefore, this work develops models of compound spiking sensors using a computational network of transduction functions and leaky integrate and fire models (together a spike encoder, the software element of a compound spiking sensor), informed by the output of an existing force transducer (hardware sensing elements of a compound spiking sensor). Force transducer failures are simulated with and without resetting between spike encoders to test the importance of resetting and configuration on compound spiking sensor durability. Fault tree analysis and discrete event simulation are used to gain a probabilistic and temporal understanding of optimal compound sensor configurations and, in specific, their effects upon durability. It was determined that the resetting of spike encoders, upon the firing of a spike by any one, was essential for allowing a compound sensor's input-output relationship to remain consistent in the face of transducer failures. Further analysis indicates that the durability of the compound sensor increases with the number of spike encoders, but decreases with the number of force transducers associated with each spike encoder. Use cases simulate how 1) a compound spiking sensor can be designed to reach a target lifetime with a defined probability and 2) how to schedule maintenance to best control the probability of unexpected failure.

5.1 Introduction

Through the application of biomimetic design, our understanding of biological sensing may help inform newly engineered systems. Recent examples in this growing field include understanding how insects use optic flow to inform navigation of unmanned aerial vehicles [61], understanding how rats move their whisker arrays to design shape extraction algorithms [62], and understanding how skin ridges interact with tactile afferents to design robotic grip control [63] and texture sensing [64]. Similarly, neural spike-based output and processing has been investigated for both rapid processing of sparse signals for image classification [65] and future interfaces between the nervous system and advanced prosthetic arms [66].

Recent work has developed a spike-based sensor system that mimics the SAI afferent with a force transducer embedded in artificial skin, coupled to a virtual spike encoder composed of a transduction function and leaky integrate and fire model [67]. Similarly, these approaches have produced spiking sensors mimicking responses of SAI, PC, and RA afferents to vibration [66]. Despite the formers success in mimicking SAI afferent force–spike transformations, for use in neural prosthetics or biomimetic robotics, the system couples a single transducer to a single spike encoder. In contrast, the SAI end organ couples multiple transducer elements (Merkel cell–neurite complexes) with multiple spike encoders (spike initiation zones) [8]. These multiple spike encoders are thought to reset each other, i.e. a spike generated at any spike encoder antidromically propagates to all other spike encoders, initiating absolute refractory periods and restarting the process of spike initiation [38]. A likely benefit of the SAI end organ's compound nature has been suggested as increasing the durability of the natural mechanosensory unit [68].

For artificial sensors, durability can be defined as the ability to perform the same input-output transformation despite some level of damage to the sensor. In terms of a compound spiking sensor, where physical force transducers are tied to an A/D converter to provide input to virtual spike encoders, durability can be defined as the ability to produce the same output for a given stimulus, even though a number of the physical force transducers have failed.

Here, we model compound spiking sensors, based upon the SAI end organ, seeking to obtain design patterns for increased durability. We hypothesize that resetting between spike encoders will be an essential mechanism to durability, and that of the repeated elements in the compound spiking sensor, the number of spike encoders will be of greatest importance, compared to the number of transducers grouped to each spike encoder.

5.2 Methods

This work develops models of compound spiking sensors using a computational network of transduction functions and leaky integrate and fire models, driven by an existing force transducer. To test our hypothesis that resetting and the number of spike encoders are essential to compound sensor durability, we use this model to simulate random transducer failures with and without resetting. Next, we examine the simulation results to derived rules governing compound sensor failure, and analyze these rules with fault trees to gain a probabilistic understanding of how a compound sensor's configuration influence its durability. Finally, we use discrete event simulation derived from the fault tree to illustrate example cases of compound sensor design and use.

Compound sensors. A diagram comparing the single spiking sensor of Kim and Gerling [67] and the compound sensors simulated here is shown in figure 5.1. Force readings from a single transducer are used here, and the simplifying assumption of identical behavior is used in simulating multiple force

transducers. Data from one or more force transducers then serves as input to multiple spike encoders, each composed of a transduction function (Eqn. 3.1) and leaky integrate and fire model (Eqn. 3.2). Except when disabled, a generated spike causes all leaky integrate and fire models to reset and enter a 1 ms refractory period. In contrast, when resetting is disabled, the output of the compound spiking sensor is the superposition of spiking from all associated spike encoders. Leaky integrate and fire parameters were τ =71.409 ms, C =9.7e^{-7} mF, and $\overline{v}$ =47.3 mV, matching those in the single spiking sensor [67], and transduction parameters were set such that the summed current from multiple transducers would produce identical spiking. Therefore, all simulated sensor configurations, when undamaged, perform identical input-output transformations. The resulting transduction parameters for configurations used here are given in table 5.1.

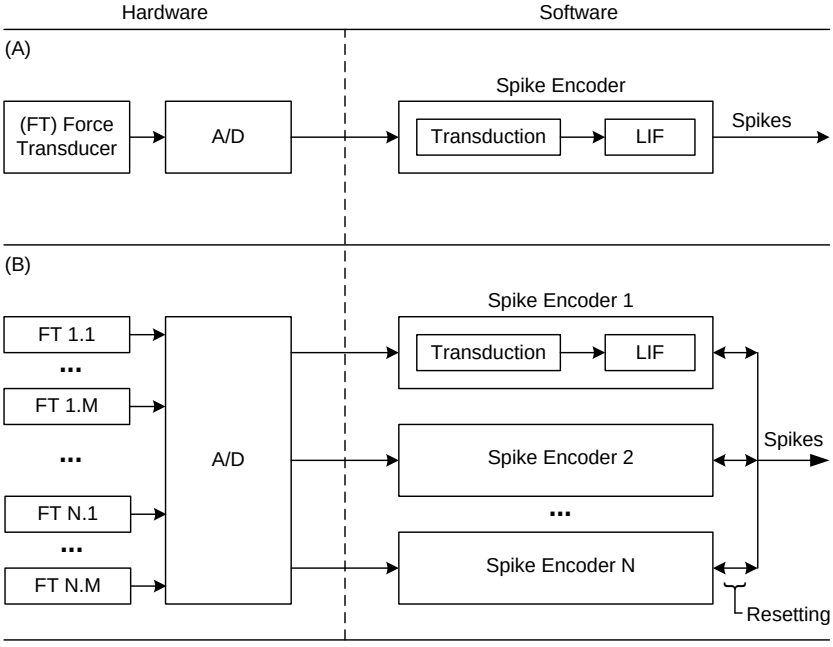

Figure 5.1: Diagram of Kim and Gerling's spiking sensor (A) where a force transducer embedded in artificial skin connected to an analog to digital converter drove a spike encoder running in software that was composed of a transduction function and leaky integrate and fire model. A comparable compound sensor is shown in (B), where N spike encoders receiving input from M transducers each. In the simulations run here, duplicates of the force readings from the hardware portion of (A) served as inputs to the software portion of (B). A/D represents the analog to digital converter.

Table 5.1: Transduction parameters for each compound sensor configuration for output identical to that of Kim and Gerling for the same input.

Configuration	β (mA)	α (mA/N)	λ (mA·S/N)
{12}	2.72 x10^{-8}	0.5167 x10^{-7}	0.22583 x10^{-4}
{6, 6}	2.72 x10^{-8}	1.0333 x10^{-7}	0.45167 x10^{-4}
{4, 4, 4}	2.72 x10^{-8}	1.5500 x10^{-7}	0.67750 x10^{-4}
{3, 3, 3, 3}	2.72 x10^{-8}	2.0667 x10^{-7}	0.90333 x10^{-4}

Simulating transducer failures with and without resetting. To test the importance of resetting and to gain insight into how the grouping of transducers to spike encoders influences compound sensor durability, simulations were run for four spiking sensor configurations: {12}, {6, 6}, {4, 4, 4}, and {3, 3, 3, 3}, where the notation represents compound spiking sensors with 1, 2, 3, and 4 spike encoders, each of which is linked to 12, 6, 4, and 3 force transducers, respectively. Even distributions of transducers to spike encoders, as compared to the uneven distribution of Merkel cells to spike initiation zones in the SAI end organ, are assumed for the artificial sensor systems simulated here. For each of the four configurations, models with and without resetting were examined. Note that the model configured {12} is identical with or without resetting, as there is a single spike encoder. Transducers were simulated as randomly failing one at a time, up to 6 failures in total, where a failure is defined as a transducer no longer outputting analog voltage to the A/D converter. A compound sensor failure was defined as any change in its input-output relationship. This was repeated five times for each configuration, with a different random set. If resetting is an essential mechanism in the durability of a compound spiking sensor, then a single transducer failure with resetting disabled would result in a changed input-output transformation (a compound sensor failure). Similarly, if the configuration of the compound sensor influences its durability, then some spiking sensor configurations should be able to tolerate more transducer failures than others before failing.

Analyzing the impact of compound sensor configuration on durability. To determine how compound sensor durability is influenced by a compound sensor's configuration, the simulation results were further examined to determine rules governing the maximum and minimum number of transducers that can fail before the overall compound sensor fails. These rules were then visualized through fault trees to give a probabilistic understanding of how the number of spike encoders and transducers associated with each influences compound sensor durability.

Discrete event simulation of use cases. The understanding obtained through the fault tree analysis was used in discrete event simulations of two cases where compound spiking sensors may be used. These cases illustrate how understanding the durability of a compound spiking sensor as transducers fail can inform 1) the number of transducers a compound spiking sensor requires to reach a target lifetime, and 2) how often to schedule maintenance to control the probability of failure. These use cases illustrate the temporal aspects of compound spiking sensor durability.

Use case simulations were coded in python, and each transducer in the simulated compound spiking sensor drew its time to failure from an exponential distribution using the built in random library. Based on the fault tree analysis, the lifetime of the compound spiking sensor was defined as the maximum life of the associated transducers. Probabilities of reaching target lifetimes were obtained by observing the outcome of 100,000 trials.

5.3 Results

Simulations of transducer failures with and without resetting. When resetting between spike encoders is disabled, a single transducer failure changes the input-output transformation of the compound sensor, regardless of configuration (Fig 5.2). This suggests resetting between spike encoders is an essential mechanism for compound spiking sensors to be robust to transducer failures. Note that

the response actually increases for the initial transducer failures. This is due to spikes that would have been masked in the undamaged case becoming discernible in the output when one or more spike encoders are firing at different frequencies (Fig 5.3). In contrast, resetting allows more than one transducer to fail before the compound spiking sensor fails for configurations of {6, 6}, {4, 4, 4}, and {3, 3, 3, 3}, Specifically, 1, 2, and 3 transducers could fail, respectively, before the compound sensor's input-output transformation changed (Fig 5.4). Note the configuration of {12}, with one spike encoder, exhibited changes in its input-output relationship with a single transducer failure.

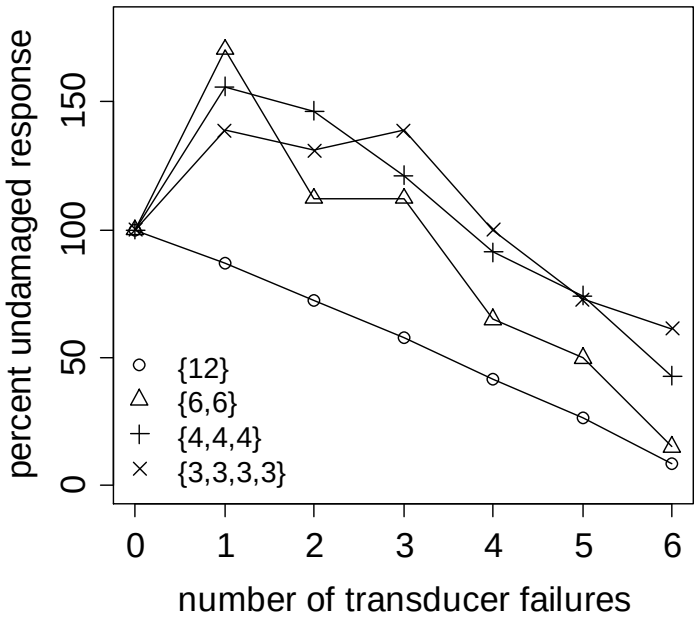

Figure 5.2: Percent undamaged response vs. number of transducer failures for 4 compound spiking sensor configurations when resetting between spike encoders is disabled. Results are averaged over 5 random orders of transducer failure. Note that the output changes with a single transducer failure regardless of configuration.

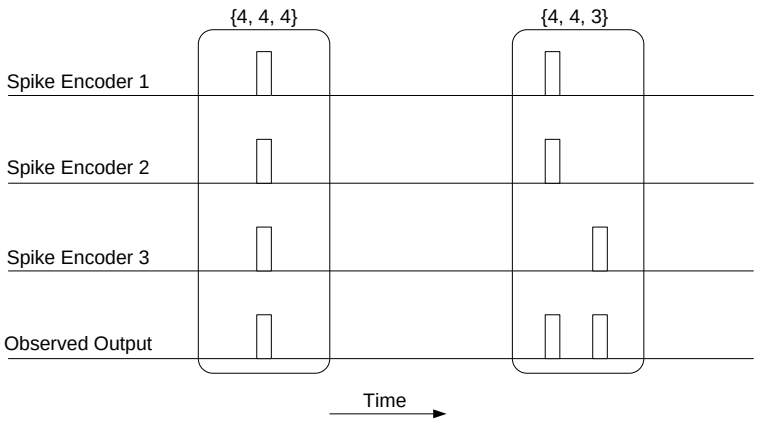

Figure 5.3: Example of how simultaneous spikes mask each other when resetting is disabled, underlying an increase in firing rate when transducers are damaged as the spike encoder with one fewer functioning transducer fires out of sync with the spike encoders with undamaged complements of transducers.

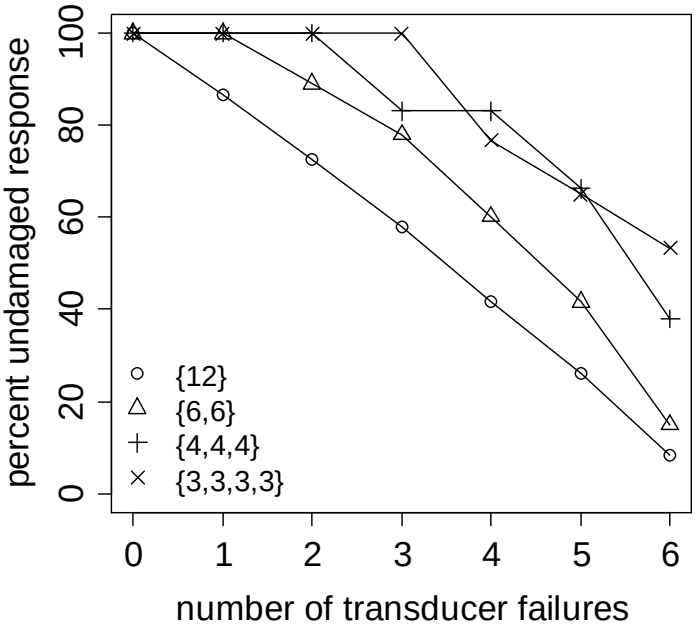

Figure 5.4: Percent undamaged response vs. number of transducer failures for 4 compound spiking sensor configurations. Results are averaged over 5 random orders of transducer failure. Note that 100% indicates no change in output while 0% indicates no output. Note that configurations of {12}, {6, 6}, {4, 4, 4} and {3, 3, 3, 3} do not have altered output until 1, 2, 3, and 4 transducers are damaged, respectively, and that this matches the associated number of spike encoders.

Examining the configurations before and after the overall failure for the five random orders of transducer failure indicates that a compound sensor with resetting does not fail until each spike encoder has had its functioning number of transducers reduced (table 5.2). In other words, as long as there is one spike encoder with an undamaged complement of transducers, the compound spiking sensor's input-output relationship remains unchanged.

Table 5.2: Transition points for simulated compound spiking sensors as transducers fail, showing the complement of transducers per spike encoder before the compound sensor output changes, and after. The spike encoder where the instigating transducer failed is underlined. Results are shown for the five random orders of sensor failure. Note that the third random order for the starting configuration of {3, 3, 3, 3} had a spike encoder with three associated transducers after six transducer failures, and that as a result the compound sensor's output did not change.

{6, 6}		**{4, 4, 4}**		**{3, 3, 3, 3}**	
Before	**After**	**Before**	**After**	**Before**	**After**
{5, 6}	{5, 5}	{3, 4, 3}	{3, 3, 3}	{3, 2, 2, 2}	{2, 2, 2, 2}
{6, 4}	{5, 4}	{4, 2, 2}	{3, 2, 2}	{3, 2, 2, 1}	{2, 2, 2, 1}
{5, 6}	{5, 5}	{3, 4, 3}	{3, 3, 3}	{1, 2, 0, 3}	NA
{6, 3}	{5, 3}	{4, 1, 2}	{3, 1, 2}	{3, 1, 1, 2}	{2, 1, 1, 2}
{4, 6}	{4, 5}	{2, 4, 2}	{2, 3, 2}	{2, 2, 3, 2}	{2, 2, 2, 2}

Analyzing the impact of compound sensor configuration on durability. Recall that simulations indicate that a compound spiking sensor fails after each spike encoder has had at least one associated transducer fail. This result suggests that for a compound spiking sensor with N spike encoders, each of which receives input from M transducers: 1) a minimum of N transducers must fail before the compound sensor fails, and 2) a maximum of M(N-1) transducers can fail before the compound sensor fails. This can be visualized as a fault tree for a compound sensor with N spike encoders each with M transducers (Fig. 5.5). If a single transducer is associated with each spike encoder, a simplified fault tree is obtained (Fig. 5.6).

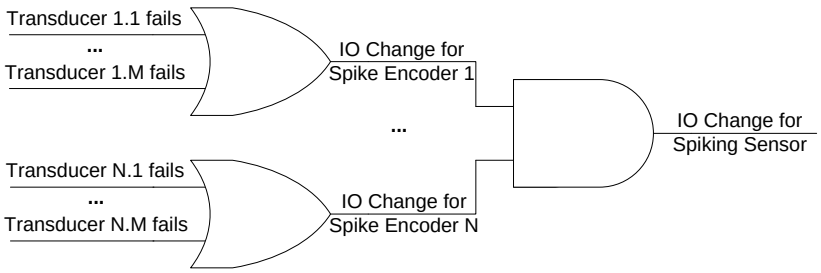

Figure 5.5: Fault tree for compound spiking sensor with N spike encoders receiving input from M transducers each.

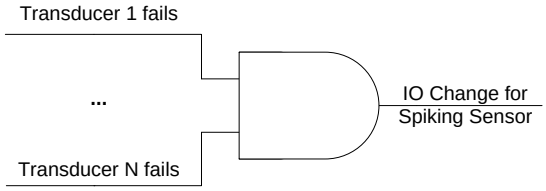

Figure 5.6: Fault tree for a compound sensor with N spike encoders receiving input from one transducer each.

Inspection suggests that the more spike encoders the more durable the compound sensor, but the more transducers associated with each spike encoder the less durable the compound sensor. For example, if the probability of a transducer failing is 0.01, then the probability of failure for a compound spiking sensor with two spike encoders, each with two transducers, is given by equation 5.1, where P(x.y) denotes the probability of failure for transducer y of spike encoder x. This results in a 0.000396 probability of failure for the compound spiking sensor.

$$P(compound\ \ fail) = (P(1.1) + P(1.2) - P(1.1 and 1.2)) \bullet (P(2.1) + P(2.2) - P(2.1 and\ 2.2)) \quad \text{Eqn 5.1}$$

Alternatively, if one transducer is associated with each spike encoder, then the overall probability of failure is given by equation 5.2, resulting in a 0.0001 probability of failure.

$$P(compound\ \ fail) = P(1.1) \bullet P(2.1) \quad \text{Eqn 5.2}$$

In this case, doubling the number of transducers grouped to each spike encoder increased the overall probability of failure almost fourfold. Therefore, it is recommended that a single transducer be linked to each spike encoder in practice.

Use Case Simulation 1: Designing for a target lifetime. A mars rover is being designed using spike based sensing and will have a mission of three years. A robotic arm for sample collection will be instrumented with a compound spiking sensor providing feedback on grip force. If the force transducers available have exponentially distributed lives with expectations of of 2, 3, and 4 years, how many transducers of each type would be required for a compound spiking sensor to achieve a 3 year lifetime with 99% confidence?

Discrete event simulation reveals that for transducers with expected lives of 2, 3, and 4 years, 8, 11, and 19 are required for the compound sensor to last the three year mission with a 0.99 percent certainty (Fig 5.7).

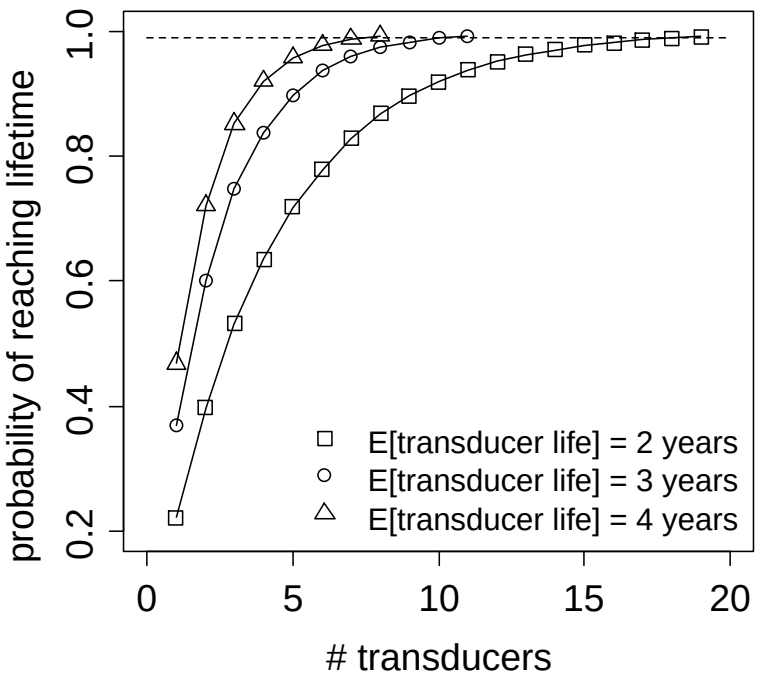

Figure 5.7: Probability of a compound spiking sensor lasting through the three year mission as a function of the number of transducers (and therefore spike encoders) used. Results are shown for transducers with expected lives of 2, 3, and 4 years. The horizontal dashed line denotes a probability of 0.99.

Use Case Simulation 2: Scheduling maintenance. An upper limb neural prosthesis provides tactile feedback using a compound spiking sensor on the thumb. Due to size constraints, only 4 force transducers can be used for this sensor. If force transducer lives are exponentially distributed with an expected lifetime of 2 years, how often should maintenance be scheduled? Maintenance must be scheduled often enough that there is a low probability that artificial touch will fail at a critical time, such as while holding a child, but not so often as to be an inconvenience or unnecessary expense to the prosthetic user.

Discrete event simulation can illicit options for the prosthetic user to consider. For example, to have no unexpected failures between scheduled maintenance with probabilities of 0.99, 0.95, and 0.90, maintenance should be scheduled for every 9, 15, and 19 months, respectively (Fig 5.8).

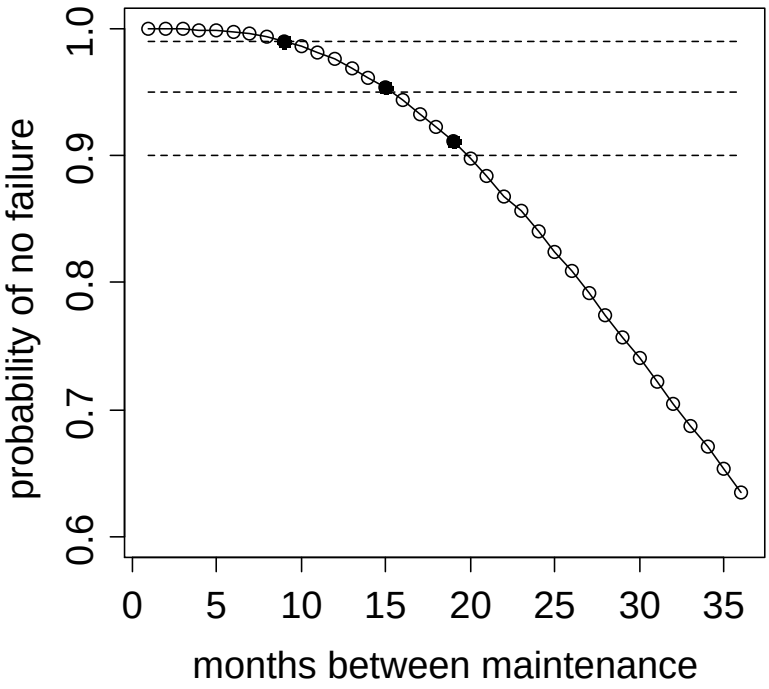

Figure 5.8: Probability of the prosthetic's compound spiking sensor surviving the interval between scheduled maintenance as a function of months between maintenance. The horizontal dashed lines denote probabilities of 0.99, 0.95, and 0.90.

5.4 Discussion

This work simulates compound spiking sensors as a more durable alternative to single spiking sensors [67], and indicates that when designing artificial sensors that mimic the compound nature of the SAI end organ, the most important design elements are multiple spike encoders and resetting between them. In terms of resetting, simulations revealed that when multiple spike encoders in a compound sensor reset each other, more than one transducer can fail before the compound sensor fails. Alternatively, when resetting is disabled, a single transducer failure results in a compound sensor failure. In terms of the configuration of a compound spiking sensor influencing its durability, fault tree analysis revealed that the while the probability of a compound spiking sensor failing decreases with the number of spike encoders, it increases with the number of transducers grouped to each spike encoder.

Note that compound spiking sensors are distinct from using a population of single spiking sensors. While compound spiking sensors, as discussed here, provide a single reading on the force value at a single location, a population of single spiking sensors provides multiple readings which require more extensive processing to interpret. Additionally, while populations of single spiking sensors could be arranged such that they provide multiple readings at the same location, populations of sensors are more likely to be leveraged to obtain spatial information for shape or texture discrimination, similar to populations of tactile afferents [69][70].

This biomimetic work is inspired by the compound nature of the SAI end organ. Guclu speculated that SAI afferents innervate multiple Merkel cells so SAI afferents can continue responding to stimuli despite the loss of one or more of these biological transducers [68]. Furthermore, immunostaining reconstructions reveal multiple biological spike encoders (spike initiation zones) [8]. While this work focused on using the SAI end organ as inspiration for more durable spiking sensors, it raises the question: if more transducers connected to spike encoders decrease a compound spiking sensor's durability, why would multiple Merkel cells be grouped to spike initiation zones in the biology? In the case of artificial sensors explored here, it is possible to arbitrarily change the parameters of the transduction function in order to obtain the desired input-output relationship, regardless of how many transducers are grouped to a spike encoder. This may not be the case biologically, and there may be a tradeoff where multiple Merkel cells increases sensitivity, but at the cost of reduced robustness.

5.5 Acknowledgments.

This work would not be possible without the contributions of colleagues in Dr. Gregory Gerling's lab. In particular, force transducer data was provided by Elmer Kim. Furthermore, this work was greatly improved through discussions with Dr. Gregory Gerling and Yuxiang Wang.

6. Conclusions and Future Directions

This work developed reconfigurable models of the SAI afferent end organ embedded in skin by combining leaky integrate and fire models of spike initiation, transduction functions representing clusters of Merkel cells, and finite element models representing the skin in which they are embedded. This approach allowed combining recent results from electrophysiological recordings of SAI afferent stimulus-response transformations and 3D confocal reconstructions of SAI end organ structure. To the best of our knowledge, this represents the first effort to model the end organ structure of the SAI afferent as well as its interaction with skin.

Using this model, two studies were undertaken to increase our understanding of how end organ structure and skin properties interact to influence the SAI afferent response. First, we investigated how the SAI stimulus-response transformation is influenced by the number of Merkel cells in its end organ as well as their grouping to spike initiation zones. Results indicated that SAI afferent firing rates increase with the number of Merkel cells in the end organ, but that this effect can be obscured by the grouping of Merkel cells to spike initiation zones. Specifically, firing rate appears to increase with the size of the largest cluster of Merkel cells, regardless of the total number of Merkel cells. Second, we investigated how changes to the SAI end organ and the skin thickness over the hair cycle impact the SAI afferent response. It was found that while firing rate increases due to active-stage end organs having more Merkel cells than rest-stage end organs, a corresponding decrease is caused by active-stage skin being thicker than rest-stage skin, suggesting skin and end organ interactions may stabilize SAI afferent stimulus-response transformations.

While the model developed here reflects the number of Merkel cells and spike initiation zones in a SAI end organ, as well as the grouping of Merkel cells to spike initiation zones, there are structural aspects of the SAI end organ not modeled here. For example, the SAI end organ has multiple nodes of

Ranvier, downstream from spike initiation zones and located at points of convergence in the SAI afferent arbor. Future work could extend the end organ model described here to reflect these propagation nodes, perhaps through adding a network of Spike Response Models which readily accept spikes as input [23]. This may allow investigating the contribution of SAI end organ structure on inter-spike interval irregularity [38]. Furthermore, reconstruction experiments reveal that the arbor simplifies with age *(Unpublished, Marshall and Lumpkin)* [55], the impact of which is not currently understood.

In addition to increasing our understanding of tactile sensing in the biology, this work sought to extend this knowledge to engineered systems. Specifically, we investigated how mimicking structural elements of the SAI end organ, such as multiple transducers and spike encoders, may lead to more durable spiking sensors. It was found that compound sensor durability increased with resetting and the number of spike encoders, but decreases with the number of transducers associated with each. Though this modeling effort was informative, future efforts in compound spiking sensor construction and application will be required to elicit practical considerations.

Using computational methods to gain insight into biological mechanisms that cannot yet be directly observed, is an emerging paradigm, one this work fits well in. Such explorations in modeling space provide predictions to test as hypotheses in empirical space. Therefore, future work may empirically test the impact of Merkel-cell grouping on the SAI afferent response, perhaps through developing a method to perform electrophysiological recordings followed by end-organ reconstructions for the same SAI afferent. While the focus of this work was to understand the role of the end organ in SAI afferent responses, the modeling approaches may be of broader interest. For example, there is evidence that both muscle spindles and tendon organs have multiple spike initiation zones[50][71][72], similar to the SAI end organ, and may be similarly modeled.

Appendix A: A Computerized Displacement Controlled Indenter.

At the start of our collaboration with Dr. Ellen Lumpkin's lab, there was a need for repeatable mechanical stimulation with a range of displacement depths and ramp-times. To address this, I designed, constructed, and integrated a computer controlled indenter with the existing apparatus at Dr. Lumpkin's Lab. In addition to eliciting constraints and requirements for the initial design through discussion, refinement and integration of the indenter was informed by a lab exchange for observing the existing surgical and electrophysiological workflow. This indenter has proven invaluable to the joint efforts between the labs of Dr. Ellen Lumpkin and Dr. Gregory Gerling [67][7][54][73][74][75].

The indenter mounts a 3 mm diameter MACOR (corning) filleted cylinder to a motorized Z-stage driven by a linear actuator (Model D-A.25AB-HT17-2-BR/4; Ultra Motion) wired in parallel to a stepper motor controller (Model 3540i; Applied Motion Products) configured for $2x10^4$ steps per revolution. The indenter has a maximum travel of 50 mm and moves in 0.32 µm increments. Accelerations up to 1.27 $\mu m/ms^2$ can be commanded. A digital signal from the motor controller was sampled to mark the onset and termination of probe movement. During mechanical stimulation, the applied force is monitored by a load cell mounted inline with the probe tip (Model 31; Honeywell) and amplified via an inline amplifier (Model 060-6827-02; Honeywell). The indenter is controlled via handheld remote or custom software.

Due to the large amount of EMF a stepper motor and controller can generate, and the sensitivity of the electrophysiological recording equipment the indenter is integrated with, shielding was a significant concern. The motor controller and power supply are mounted in a metal enclosure which is grounded, as is the Z-stage and stepper motor. When possible, shielded cable was used. When shielded cable could not be used, for the preexisting wires connecting directly to the motor for example, unshielded wire was wrapped in metalized cloth tape with pig-tail grounding wires along the length.

In operation, the experimenter first uses the user interface to place the indenter in manual mode, which allows using the handheld remote to position the probe at the skin surface. After using the handheld remote to exit manual mode, the experimenter then uses the user interface to back the probe off the skin a distance specified by the experimental protocol, 0.5 mm for the experiments here. At this point the user uses the user interface to specify stimuli to run. When the user initiates a specified stimulation in the user interface, the software communicates over a RS 232 serial connection with the motor controller. Commands from the control software first pause execution of the motor controller's command queue, buffers the SCI commands required for the specified indentation, then resumes execution of the command queue. The motor controller provides the appropriate signals to the motor and provides a signal to the recording apparatus signifying the start and stop of all movements. Figure A.1 shows the integration of the indenter with the existing apparatus (A), and an image of the motorized Z stage with probe and inline force transducer.

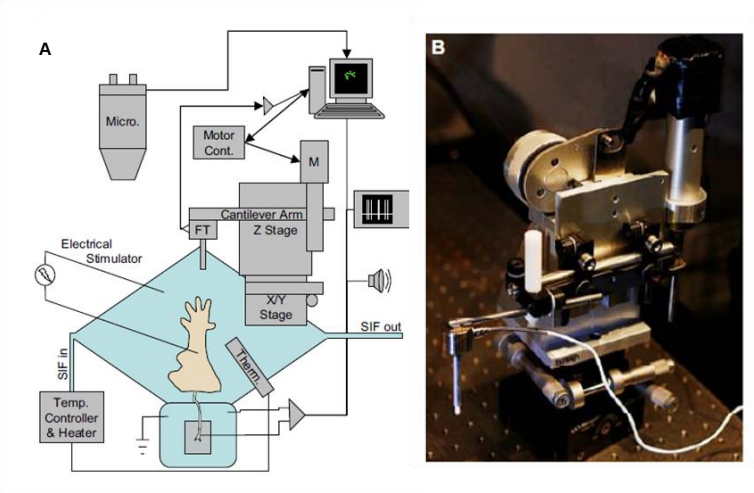

Figure A.1: (A) Diagram of computerized indenter (composed of the Z-stage, force transducer (FT), motor controller, and motor (M)) integrated with existing electrophysiology apparatus. (B) Photo of motorized Z-stage with probe and inline force transducer. Image adapted from [7].

The user interface for the indenter control software was composed of three panels: the logging panel (fig A.2A), the Fine control panel (fig A.2B), and the standard stimuli panel (fig A.2C). The logging

panel allows the experimenter to start automatic timekeeping and logging of stimuli. The fine control panel allows arbitrary probe movements to be specified, and also facilitates entering manual mode. Finally, the standard stimuli panel presents standard options for the experimental protocol used here, allowing for simpler control with less risk of user error. Stimuli are specified as a displacement and acceleration. The control software was written in C# using sharp develop version 2.2.1, build 2648, and an executable was compiled for use on the experimenter computer.

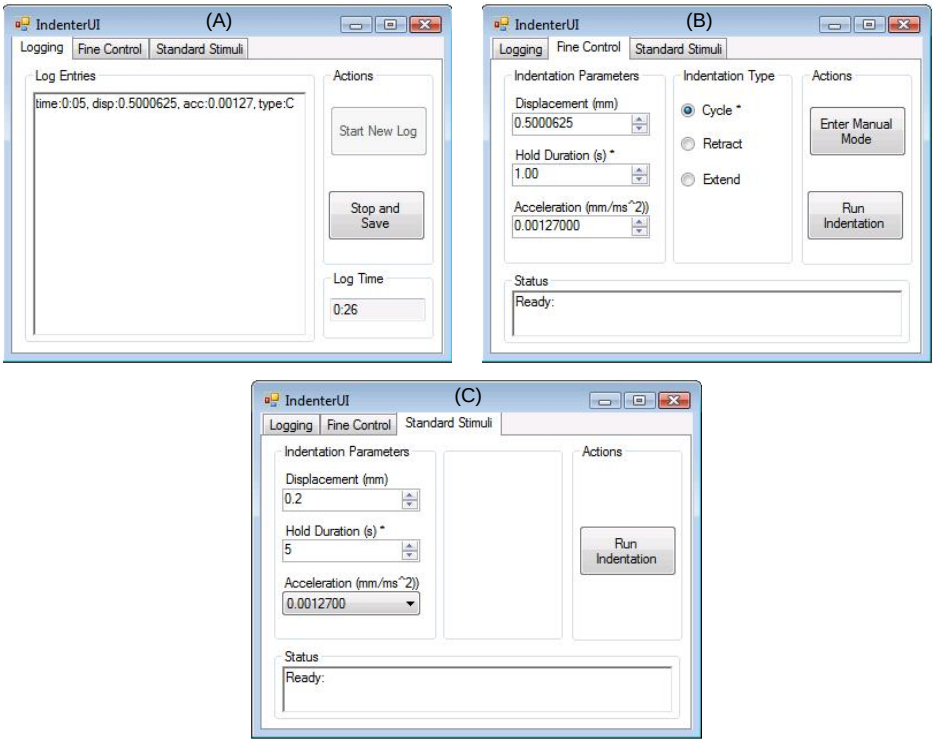

Figure A.2: User interface for indenter, showing the logging panel (A), fine control panel (B), and standard stimuli panel (C).

The indenter is an open loop system, and deviations may exist between commanded and achieved displacements. Factors such as deformation of the load cell, fluid levels, and motor performance may contribute to such slack, making it necessary to estimate achieved displacements for use in the skin model. Initially, displacements were estimated using stimulus ramp times derived from

force traces, and the assumption that the commanded acceleration was achieved. However, initial laser measurements of probe movement brought the assumption of commanded acceleration into question. To address this, an experiment was run to determine the actual accelerations the indenter achieves, allowing better displacement estimates for use in our skin models.

In this experiment, a laser measurement device was installed (optoNCD 1402-5, Micro-Epsilon), and a family of displacements representative of those used in the electrophysiological recordings were tracked. Commanded displacements ranged from 1.4 to 1.8 mm in 0.1 mm increments, starting from a 0.5 mm offset from the skin. Accelerations of 0.0000254 mm/ms^2, 0.0001016 mm/ms^2, and 0.00127 mm/ms^2 were used, identical to those in question. Each unique displacement-acceleration pair was repeated three times, for a total of 45 stimulations.

For each stimulation, the ramp time, i.e. the time from the probe contacting the skin to reaching its final indentation depth, was estimated from the force trace (t). Using the start and stop times of the stimulus ramp, the achieved displacement into the skin (d) was obtained from the laser measured displacement trace. Using t, d, and the assumption of constant acceleration (deceleration into the skin), the estimated acceleration for each stimulation was obtained from equation A.1 (table A.1).

$$a = \frac{2d}{t^2} \qquad \text{Eqn A.1}$$

Table A.1 Estimated accelerations for each stimulus type. Standard deviation shown in parenthesis.

Cmd d (mm)	Cmd a (mm/ms^2)	Msrd t (ms)	Msrd d (mm)	Calc a (mm/ms^2)
1.4	0.0000254	221 (0.58)	0.48 (0.0033)	$1.97x10^{-05}$ ($2.20x10^{-07}$)
1.5	0.0000254	235 (1.53)	0.55 (0.0059)	$2.01x10^{-05}$ ($1.87x10^{-07}$)
1.6	0.0000254	254 (1.73)	0.64 (0.0232)	$1.97x10^{-05}$ ($4.48x10^{-07}$)
1.7	0.0000254	267 (1.73)	0.71 (0.0191)	$2.00x10^{-05}$ ($2.84x10^{-07}$)
1.8	0.0000254	281 (0.58)	0.77 (0.0030)	$1.95x10^{-05}$ ($1.22x10^{-07}$)
1.4	0.0001016	112 (0.58)	0.51 (0.0054)	$8.25x10^{-05}$ ($6.28x10^{-07}$)
1.5	0.0001016	118 (0.58)	0.59 (0.0060)	$8.46x10^{-05}$ ($6.64x10^{-08}$)
1.6	0.0001016	127 (0.58)	0.66 (0.0020)	$8.28x10^{-05}$ ($6.22x10^{-07}$)
1.7	0.0001016	137 (0.00)	0.73 (0.0022)	$7.83x10^{-05}$ ($2.38x10^{-07}$)
1.8	0.0001016	144 (1.15)	0.81 (0.0089)	$7.74x10^{-05}$ ($3.85x10^{-07}$)
1.4	0.00127	28 (0.58)	0.48 (0.0128)	$1.21x10^{-03}$ ($1.95x10^{-05}$)
1.5	0.00127	30 (0.00)	0.55 (0.0092)	$1.23x10^{-03}$ ($2.05x10^{-05}$)
1.6	0.00127	35 (0.00)	0.64 (0.0113)	$1.05x10^{-03}$ ($1.84x10^{-05}$)
1.7	0.00127	36 (1.00)	0.70 (0.0071)	$1.09x10^{-03}$ ($5.03x10^{-05}$)
1.8	0.00127	38 (0.71)	0.80 (0.0042)	$1.14x10^{-03}$ ($3.69x10^{-05}$)

Calculated accelerations for each stimulus were averaged by commanded acceleration to obtain the accelerations used in this body for work for displacements estimates. Calculated achieved accelerations were 0.0000198, 0.0000811, and 0.0011432 mm/ms^2, corresponding to commanded accelerations of 0.0000254, 0.0001016, and 0.0012700 mm/ms^2, respectively. These achieved accelerations yield displacement estimates much closer to laser recorded displacement traces than displacement estimates based on commanded accelerations (Fig A.3-A.5).

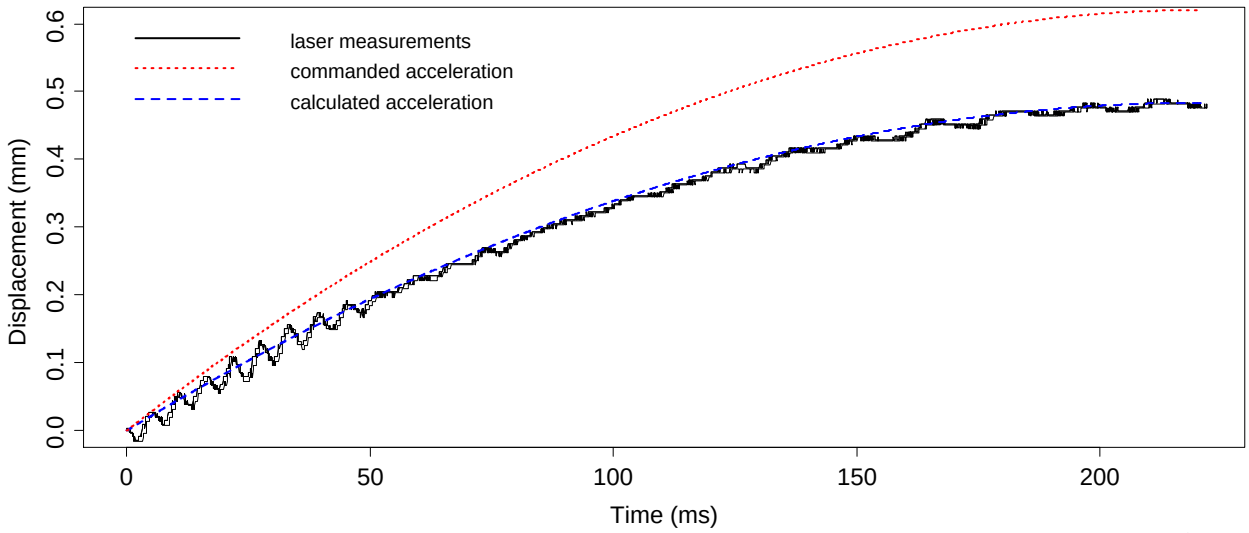

Figure A.3: Three measured ramps for stimuli with commanded accelerations of 0.0000254 mm/ms^2 and commanded displacements of 1.4 mm (black lines), simulated displacement trace using commanded acceleration (red line), and simulated displacement trace using achieved acceleration value obtained in this effort (blue line).

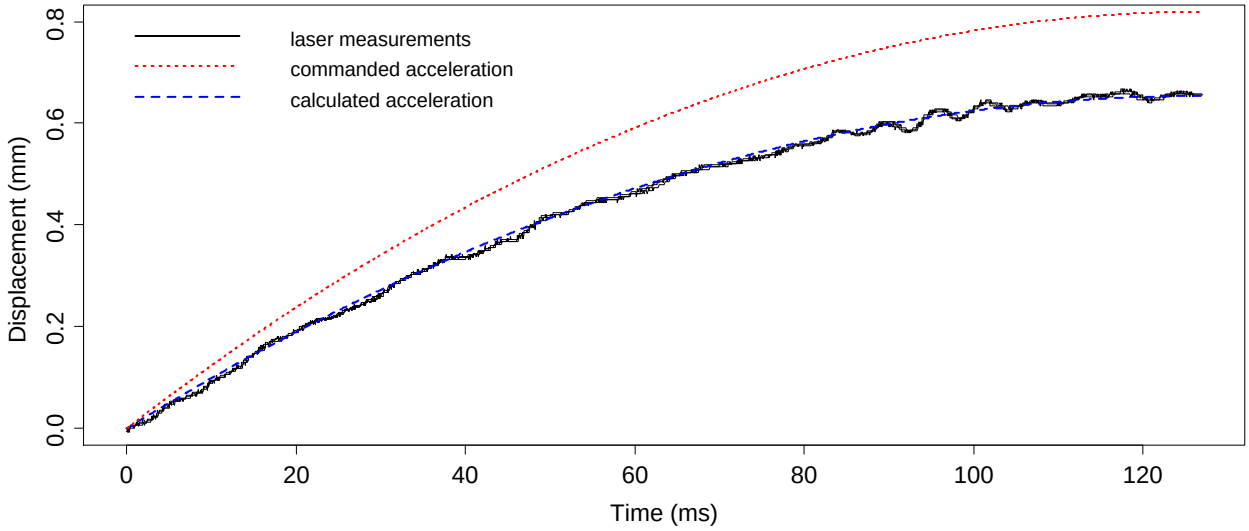

Figure A.4: Three measured ramps for a stimuli with commanded accelerations of 0.0001016 mm/ms^2 and commanded displacements of 1.6 mm (black lines), simulated displacement trace using commanded acceleration (red line), and simulated displacement trace using achieved acceleration value obtained in this effort (blue line).

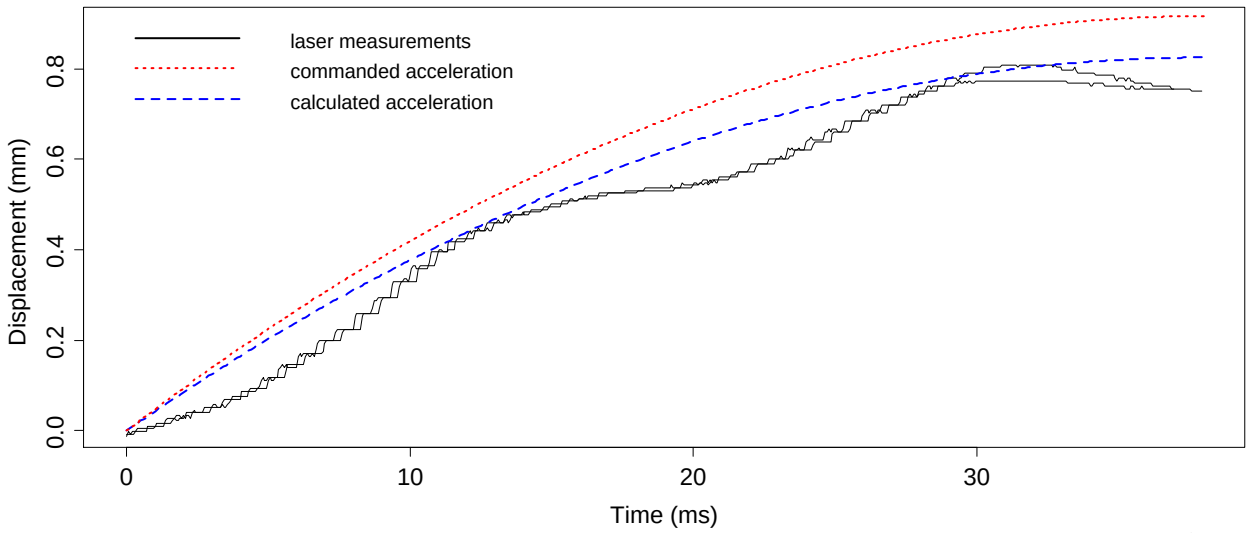

Figure A.5: Three measured ramps for a stimuli with commanded accelerations of 0.0012700 mm/ms^2 and commanded displacements of 1.8 mm (black lines), simulated displacement trace using commanded acceleration (red line), and simulated displacement trace using achieved acceleration value obtained in this effort (blue line).

In addition to obtaining accelerations for use in displacement estimates, this experiment allowed examining the assumption that displacement is consistent and independent of acceleration. The results suggest that variation in estimated displacements is introduced during the estimation, as total displacements, which can be more directly measured, are quite consistent (Fig A.6). This estimation is necessary, however, as laser measurements were not available when the electrophysiology for the work was conducted. While the effective displacements into the skin in the laser measurement experiments are greater here than in the electrophysiology for this work, it is expected that the derived accelerations are correct. This discrepancy in displacements may result from differences in initial stimulus positioning, and it should be noted that the laser measurement experiments were conducted by a different experimenter than the electrophysiological experiments.

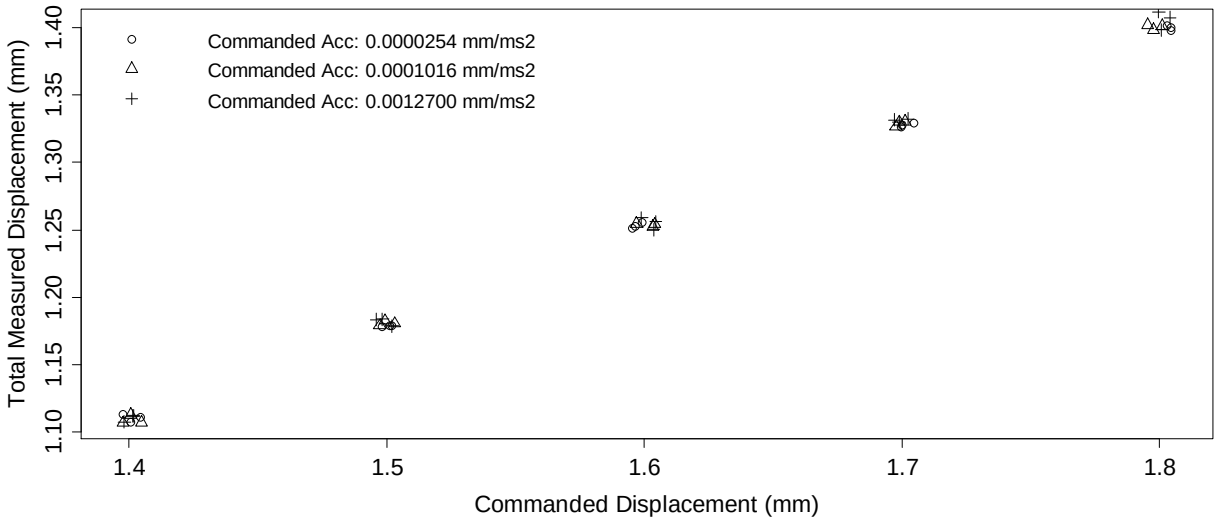

Figure A.6: Measured total displacement vs. commanded displacement.

Appendix B: Contact Detection and Displacement Estimates

Ideally, it would be possible to obtain the displacement into the skin by subtracting the initial 0.5 mm probe offset from the commanded displacement. However, due to factors such as variation in initial stimulus positioning and differences in ideal vs. actual motor performance, it is necessary to estimate the effective displacements into the skin. It is assumed the difference in ideal vs. actual motor performance is constant across preparations and sufficiently characterized in appendix A. Initial probe positioning is performed once per prep, making its impact on effective displacements constant for a single SAI afferent. Therefore, it is assumed that effective displacements into the skin are consistent for a given preparation, and can be estimated on preparation to preparation basis.

To estimate displacements, we use the accelerations obtained in appendix A, with ramp times obtained by noting the signal from the motor controller indicating the end of probe movement, and by estimating contact from the associated force traces. Though from different sources, these signals were both sampled with the same A/D card (DT304; Data Translation) and stored using the same clock via. recording software (SciWorks Experimenter 6.0; DataWave Technologies). Probe contact times were estimated from force traces through examining a 50 ms window and visually taking the first point that rose above noise. Ramp times are expected to be consistent for a given displacement, acceleration, and preparation, with variation introduced through the estimation. This allowed for examining ramp times by stimulus, then re-estimating the contact times associated with ramp times that differed. The standard deviation of resulting ramp times, by stimulus, was under 2 ms (Tables B1, B3, B5, and B7).

The probes movement is sigmoidal, i.e. for the first half of movement the probe is accelerating and for the second half it is decelerating. As the time from probe movement to contact is consistently larger than the time from contact to when the probe stops, it is expected that as the probe is moving

into the skin, it is constantly decelerating. This suggests simple kinematics with constant acceleration can be used in estimating displacements from ramp times. The displacement of a probe contacting the skin with an initial velocity V_i and decelerating with acceleration a for a period of time t is given by equation B.1.

$$d = V_i t - \frac{1}{2} a t^2 \qquad \text{Eqn B.1}$$

Note that at the end of t, the probe stops moving and comes to rest at its final displacement. The problem of estimating displacement can therefore be simplified due to symmetry. We can obtain d by solving the problem of how far the probe would move out of the skin from rest, with the same acceleration. This gives equation B.2, which was used in estimating displacements using t defined as the difference in probe stop times and estimated contact times, and using the accelerations obtained in appendix A.

$$d = \frac{1}{2} a t^2 \qquad \text{Eqn B.2}$$

The results of these displacement estimates are shown for the four skin-nerve preparations used in this work (Tables B1, B3, B5, and B7). Recall that displacements differ from commanded displacement, but are consistent for a given preparation and are independent of acceleration. Therefore, displacements were averaged across accelerations for each preparation (Tables B2, B4, B6, and B8). Displacement estimates cluster fairly well, and while there are some differences in estimates by acceleration, it is expected that these are introduced by the estimation procedure (Fig B1, B2, B3, and B4).

Table B.1 Estimated displacement by stimulus type for fiber 290509 (Recording D). Standard deviation shown in parenthesis.

Commanded Disp (mm)	Acceleration (mm/ms^2)	N	Ramp Time (ms)	Estimated Disp (mm)
1.4	0.0000198	1	73 (NA)	0.05 (NA)
1.5	0.0000198	4	116 (1.91)	0.13 (0.0044)
1.6	0.0000198	4	145 (1.15)	0.21 (0.0033)
1.7	0.0000198	4	168 (1.73)	0.28 (0.0058)
1.8	0.0000198	2	186 (0.71)	0.34 (0.0026)
1.4	0.0000811	1	34 (NA)	0.05 (NA)
1.5	0.0000811	4	61 (1.50)	0.15 (0.0074)
1.6	0.0000811	4	76 (1.73)	0.24 (0.0108)
1.7	0.0000811	4	88 (0.58)	0.32 (0.0041)
1.8	0.0000811	2	94 (0.00)	0.36 (0.0000)
1.4	0.0011432	1	10 (NA)	0.06 (NA)
1.5	0.0011432	4	16 (0.82)	0.15 (0.0149)
1.6	0.0011432	4	20 (0.96)	0.23 (0.0219)
1.7	0.0011432	4	24 (0.00)	0.33 (0.0000)
1.8	0.0011432	2	26 (0.71)	0.37 (0.0206)

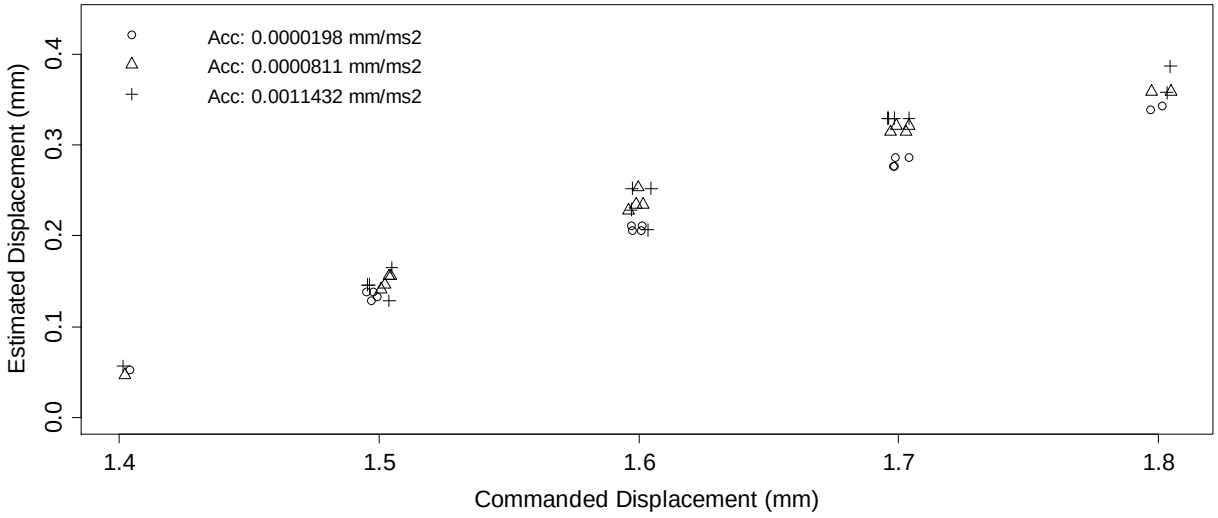

Figure B.1: Estimated vs. commanded displacement for fiber 290509.

Table B.2 Estimated displacements averaged over commanded displacement for fiber 290509 (Recording D). Standard deviation shown in parenthesis.

Commanded Disp (mm)	N	Estimated Disp (mm)
1.4	3	0.052 (0.0052)
1.5	12	0.144 (0.0113)
1.6	12	0.227 (0.0189)
1.7	12	0.309 (0.0217)
1.8	6	0.357 (0.0168)

Table B.3: Estimated displacement by stimulus type for fiber 220509 (Recording C). Standard deviation shown in parenthesis.

Commanded Disp (mm)	Acceleration (mm/ms^2)	N	Ramp Time (ms)	Estimated Disp (mm)
1.4	0.0000198	3	113 (0.58)	0.13 (0.0013)
1.5	0.0000198	3	135 (0.00)	0.18 (0.0000)
1.6	0.0000198	3	168 (1.00)	0.28 (0.0033)
1.7	0.0000198	3	189 (1.00)	0.35 (0.0037)
1.4	0.0000811	3	55 (0.58)	0.12 (0.0026)
1.5	0.0000811	3	70 (0.00)	0.20 (0.0000)
1.6	0.0000811	3	85 (1.15)	0.30 (0.0080)
1.7	0.0000811	3	96 (0.00)	0.37 (0.0000)
1.4	0.0011432	3	15 (0.58)	0.12 (0.0096)
1.5	0.0011432	3	18 (1.53)	0.19 (0.0324)
1.6	0.0011432	4	23 (0.82)	0.30 (0.0215)
1.7	0.0011432	3	25 (0.00)	0.36 (0.0000)

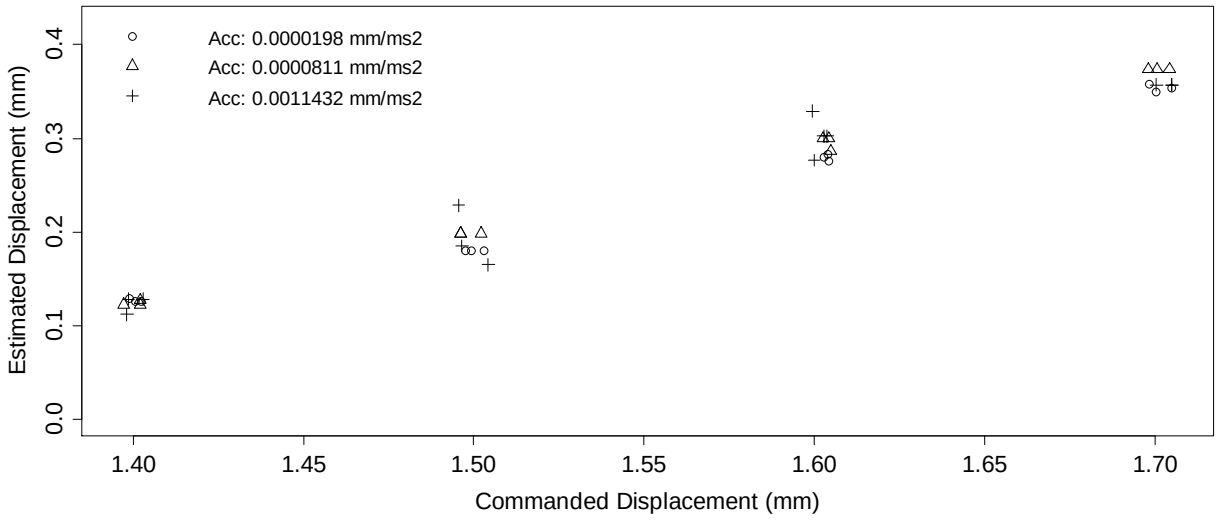

Figure B.2: Estimated vs. commanded displacement for fiber 220509

Table B.4: Estimated displacements averaged over commanded displacement for fiber 220509 (Recording C). Standard deviation shown in parenthesis.

Commanded Disp (mm)	N	Estimated Disp (mm)
1.4	9	0.125 (0.0053)
1.5	9	0.191 (0.0181)
1.6	10	0.294 (0.0166)
1.7	9	0.362 (0.0095)

Table B.5 Estimated displacement by stimulus type for fiber 200209 (Recording B). Standard deviation shown in parenthesis.

Commanded Disp (mm)	Acceleration (mm/ms^2)	N	Ramp Time (ms)	Estimated Disp (mm)
1.4	0.0000198	1	55 (NA)	0.03 (NA)
1.6	0.0000198	3	107 (1.15)	0.11 (0.0024)
1.8	0.0000198	3	162 (1.00)	0.26 (0.0032)
1.4	0.0000811	2	8 (0.71)	0.00 (0.0004)
1.6	0.0000811	3	54 (0.00)	0.12 (0.0000)
1.8	0.0000811	3	82 (0.58)	0.27 (0.0038)
1.6	0.0011432	3	15 (0.00)	0.13 (0.0000)
1.8	0.0011432	3	21 (0.58)	0.26 (0.0142)

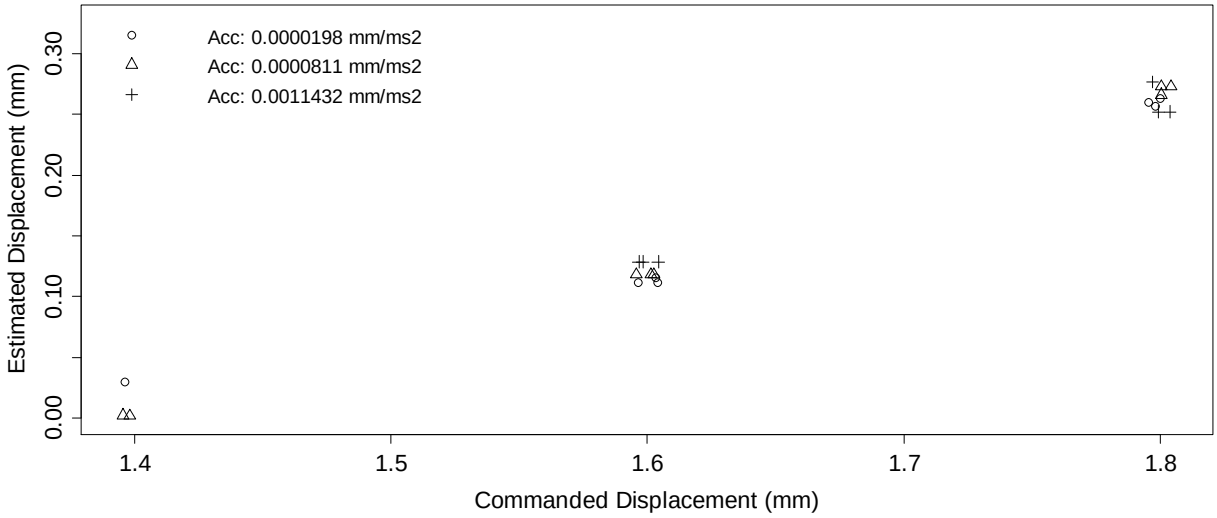

Figure B.3: Estimated vs. commanded displacement for fiber 200209

Table B.6: Estimated displacements averaged over commanded displacement for fiber 200209 (Recording B). Standard deviation shown in parenthesis.

Commanded Disp (mm)	N	Estimated Disp (mm)
1.4	3	0.012 (0.0160)
1.6	9	0.120 (0.0071)
1.8	9	0.264 (0.0092)

Table B.7 Estimated displacement by stimulus type for fiber 180209 (Recording A). Standard deviation shown in parenthesis.

Commanded Disp (mm)	Acceleration (mm/ms^2)	N	Ramp Time (ms)	Estimated Disp (mm)
1.2	0.0000198	1	31 (NA)	0.01 (NA)
1.4	0.0000198	3	45 (0.58)	0.02 (0.0005)
1.6	0.0000198	3	107 (1.15)	0.11 (0.0024)
1.8	0.0000198	3	154 (0.58)	0.23 (0.0018)
1.4	0.0000811	3	15 (0.58)	0.01 (0.0007)
1.6	0.0000811	3	58 (0.58)	0.13 (0.0027)
1.8	0.0000811	3	84 (0.58)	0.29 (0.0040)
1.4	0.0011432	3	6 (1.00)	0.02 (0.0069)
1.6	0.0011432	3	15 (1.15)	0.12 (0.0198)
1.8	0.0011432	3	21 (0.00)	0.25 (0.0000)

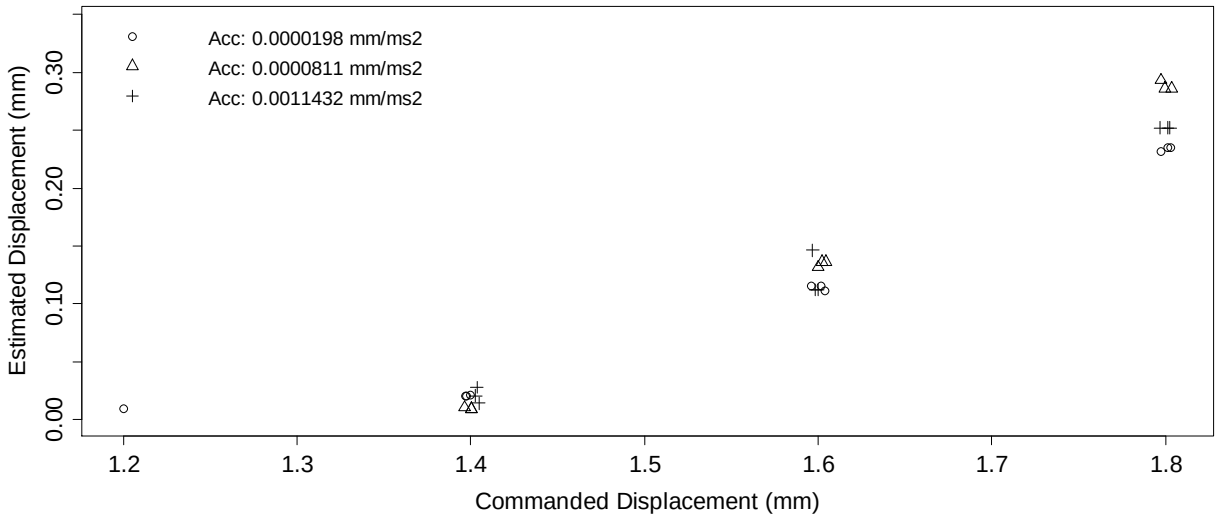

Figure B.4: Estimated vs. commanded displacement for fiber 180209

Table B.8: Estimated displacements averaged over commanded displacement for fiber 180209 (Recording A). Standard deviation shown in parenthesis.

Commanded Disp (mm)	N	Estimated Disp (mm)
1.2	1	0.010 (NA)
1.4	9	0.017 (0.0066)
1.6	9	0.124 (0.0135)
1.8	9	0.258 (0.0242)

Appendix C: Model Fitting

Recall that the four end organ models in aim 1 were fit to the mean in-vivo displacement-firing rate relationship using gradient free response surface methodology where starting regions were informed by a domain search using 50 trial points. The boundaries of the parameter domain searched are defined in table C.1, and were identical for each model configuration. After each domain search, three iterative experimental regions consisting of 20 trial points were examined. Between iterations, new experimental regions were centered on the best point from the previous experimental region, and the ranges of individual parameters were reduced to 50% what they were. Note that the center of the first experimental region differed from the best point of the domain search, in particular for λ, as additional points were taken into consideration in choosing the starting region. All space filling designs, for both the domain searches and experimental regions, were sampled via the LHS package in R.

Table C.1: Bounds of domain searches used to inform starting regions

Parameter	Min	Max
β (mA)	5.000×10^{-8}	6.000×10^{-8}
α (mA/Pa)	1.000×10^{-14}	9.000×10^{-14}
λ (mA·ms/Pa)	1.000×10^{-11}	9.000×10^{-11}

The resulting parameter values and combined fractional sum of squares are shown in table C.2. Fits ranged from 1.91 to 1.94. Intermediate results are shown in tables C.3, C.5, C.7, C.9 for fitting model configurations {8, 5, 3, 1}, {7, 6, 4, 2, 1}, {6, 4, 3}, and {5, 4, 3, 1}, respectively. Note there is some oscillation in the parameters. Experimental regions used in fitting are detailed in tables C.4, C.6, C.8, and C.10 for fitting model configurations {8, 5, 3, 1}, {7, 6, 4, 2, 1}, {6, 4, 3}, and {5, 4, 3, 1}, respectively. Overall, the resulting output was in agreement with the mean response profile fit to, and fell within the range defined by the most and least responsive SAI (Fig C1, C2, C3, and C4).

Table C.2: Final parameters and combined fractional sum of squares from model fitting. Results are shown for four model configurations specified in Aim 1.

Configuration	β (mA)	α (mA/Pa)	λ (mA·ms/Pa)	Combined FSS
{8, 5, 3, 1}	$5.643\text{x}10^{-8}$	$2.539\text{x}10^{-14}$	$5.833\text{x}10^{-11}$	1.91
{7, 6, 4, 2, 1}	$5.648\text{x}10^{-8}$	$2.386\text{x}10^{-14}$	$4.994\text{x}10^{-11}$	1.92
{6, 4, 3}	$5.669\text{x}10^{-8}$	$2.612\text{x}10^{-14}$	$6.211\text{x}10^{-11}$	1.94
{5, 4, 3, 1}	$5.672\text{x}10^{-8}$	$2.641\text{x}10^{-14}$	$6.491\text{x}10^{-11}$	1.93

Fitting Results for Configuration {8, 5, 3, 1}:

Table C.3: Best parameters from domain search and three experiment regions for model configured {8, 5, 3, 1}

Design	β (mA)	α (mA/Pa)	λ (mA·ms/Pa)	Static FSS	Dynamic FSS	Combined FSS
Domain Search	$5.565\text{x}10^{-8}$	$3.573\text{x}10^{-14}$	$5.620\text{x}10^{-11}$	0.82	0.96	1.78
Region 1	$5.633\text{x}10^{-8}$	$2.666\text{x}10^{-14}$	$6.239\text{x}10^{-11}$	0.92	0.95	1.87
Region 2	$5.645\text{x}10^{-8}$	$2.366\text{x}10^{-14}$	$6.023\text{x}10^{-11}$	0.96	0.95	1.91
Region 3	$5.643\text{x}10^{-8}$	$2.539\text{x}10^{-14}$	$5.833\text{x}10^{-11}$	0.96	0.96	1.91

Table C.4: Design ranges for three experimental regions used in fitting model configured {8, 5, 3, 1}

Design	β Min	β Max	α Min	α Max	λ Min	λ Max
Region 1	$5.555\text{x}10^{-8}$	$5.680\text{x}10^{-8}$	$2.510\text{x}10^{-14}$	$4.500\text{x}10^{-14}$	$4.000\text{x}10^{-11}$	$7.000\text{x}10^{-11}$
Region 2	$5.602\text{x}10^{-8}$	$5.664\text{x}10^{-8}$	$2.166\text{x}10^{-14}$	$3.166\text{x}10^{-14}$	$5.489\text{x}10^{-11}$	$6.989\text{x}10^{-11}$
Region 3	$5.629\text{x}10^{-8}$	$5.661\text{x}10^{-8}$	$2.116\text{x}10^{-14}$	$2.616\text{x}10^{-14}$	$5.648\text{x}10^{-11}$	$6.989\text{x}10^{-11}$

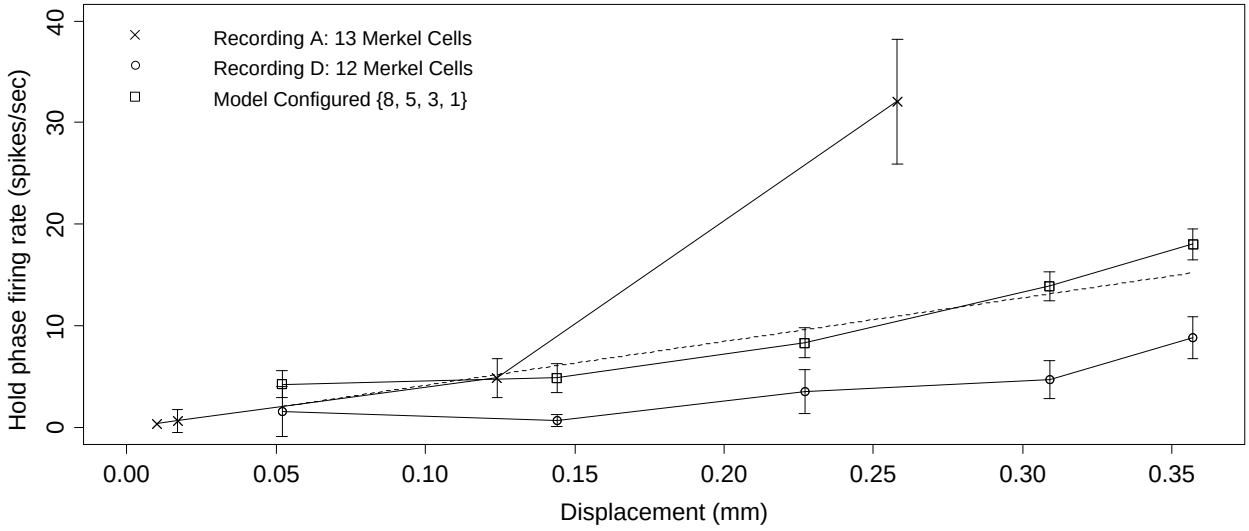

Figure C.1: Resulting displacement vs. firing rate for model configured {8, 5, 3, 1}. Note the resulting input-output relationship is in agreement with the baseline response fit to (dashed line). The most (A) and least (D) responsive SAI afferents recorded from are displayed for context, and the modeled output falls within the observed range.

Fitting Results for Configuration {7, 6, 4, 2, 1}:

Table C.5: Best parameters from domain search and three experiment regions for model configured {7, 6, 4, 2, 1}.

Design	β (mA)	α (mA/Pa)	λ (mA·ms/Pa)	Static FSS	Dynamic FSS	Combined FSS
Domain Search	5.678×10^{-8}	2.000×10^{-14}	3.509×10^{-11}	0.90	0.90	1.80
Region 1	5.638×10^{-8}	2.220×10^{-14}	5.150×10^{-11}	0.96	0.96	1.92
Region 2	5.636×10^{-8}	2.403×10^{-14}	5.229×10^{-11}	0.96	0.96	1.92
Region 3	5.648×10^{-8}	2.386×10^{-14}	4.994×10^{-11}	0.96	0.96	1.92

Table C.6: Design ranges for three experimental regions used in fitting model configured {7, 6, 4, 2, 1}

Design	β **Min**	β **Max**	α **Min**	α **Max**	λ **Min**	λ **Max**
Region 1	5.610×10^{-8}	5.741×10^{-8}	1.000×10^{-14}	3.000×10^{-14}	3.000×10^{-11}	4.000×10^{-11}
Region 2	5.607×10^{-8}	5.669×10^{-8}	1.720×10^{-14}	2.720×10^{-14}	4.400×10^{-11}	5.900×10^{-11}
Region 3	5.620×10^{-8}	5.652×10^{-8}	2.153×10^{-14}	2.653×10^{-14}	4.854×10^{-11}	5.604×10^{-11}

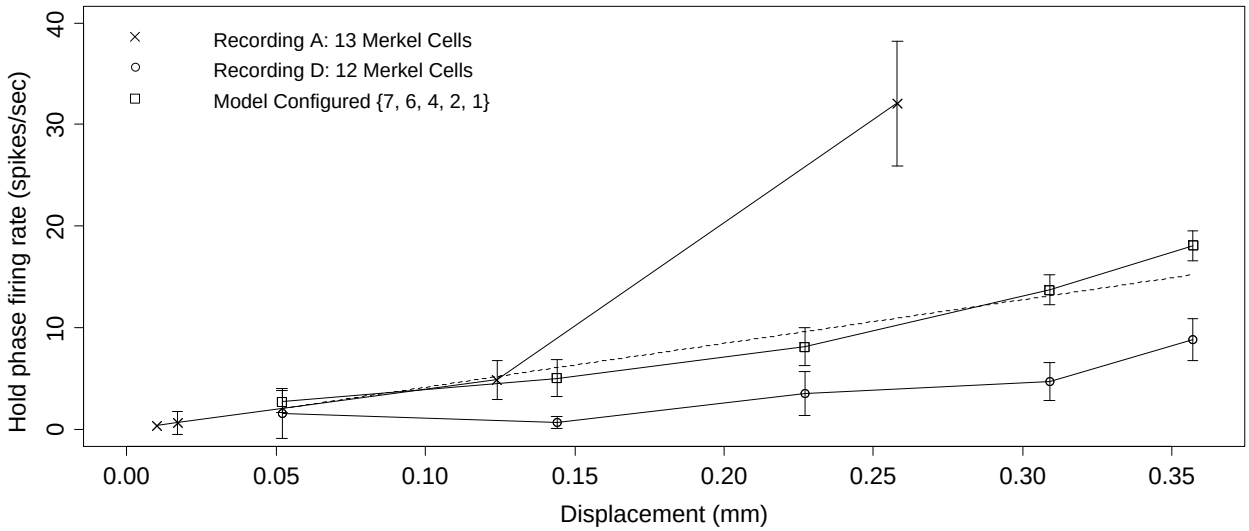

Figure C.2: Resulting displacement vs. firing rate for model configured {7, 6, 4, 2, 1}. Note the resulting input-output relationship is in agreement with the baseline response fit to (dashed line). The most (A) and least (D) responsive SAI afferents recorded from are displayed for context, and the modeled output falls within the observed range.

Fitting Results for Configuration {6, 4, 3}:

Table C.7: Best parameters from domain search and three experiment regions for model configured {6, 4, 3}

Design	β (mA)	α (mA/Pa)	λ (mA·ms/Pa)	Static FSS	Dynamic FSS	Combined FSS
Domain Search	$5.700\text{x}10^{-8}$	$2.477\text{x}10^{-14}$	$3.132\text{x}10^{-11}$	0.86	0.85	1.71
Region 1	$5.676\text{x}10^{-8}$	$2.763\text{x}10^{-14}$	$6.349\text{x}10^{-11}$	0.94	0.97	1.90
Region 2	$5.665\text{x}10^{-8}$	$2.593\text{x}10^{-14}$	$6.515\text{x}10^{-11}$	0.97	0.97	1.94
Region 3	$5.669\text{x}10^{-8}$	$2.612\text{x}10^{-14}$	$6.211\text{x}10^{-11}$	0.97	0.96	1.94

Table C.8: Design ranges for three experimental regions used in fitting model configured {6, 4, 3}

Design	β **Min**	β **Max**	α **Min**	α **Max**	λ **Min**	λ **Max**
Region 1	$5.600\text{x}10^{-8}$	$5.725\text{x}10^{-8}$	$2.400\text{x}10^{-14}$	$4.400\text{x}10^{-14}$	$4.000\text{x}10^{-11}$	$7.000\text{x}10^{-11}$
Region 2	$5.645\text{x}10^{-8}$	$5.707\text{x}10^{-8}$	$2.263\text{x}10^{-14}$	$3.263\text{x}10^{-14}$	$5.599\text{x}10^{-11}$	$7.099\text{x}10^{-11}$
Region 3	$5.649\text{x}10^{-8}$	$5.681\text{x}10^{-8}$	$2.343\text{x}10^{-14}$	$2.843\text{x}10^{-14}$	$6.140\text{x}10^{-11}$	$6.890\text{x}10^{-11}$

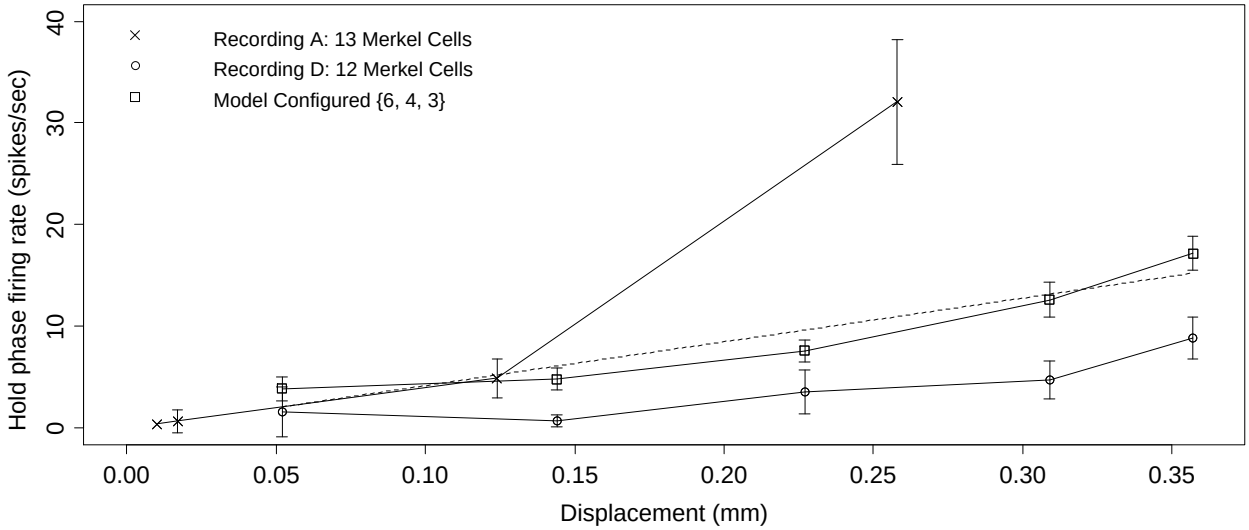

Figure C.3: Resulting displacement vs. firing rate for model configured {6, 4, 3}. Note the resulting input-output relationship is in agreement with the baseline response fit to (dashed line). The most (A) and least (D) responsive SAI afferents recorded from are displayed for context, and the modeled output falls within the observed range.

Fitting Results for Configuration {5, 4, 3, 1}:

Table C.9: Best parameters from domain search and three experiment regions for model configured {5, 4, 3, 1}

Design	β (mA)	α (mA/Pa)	λ (mA·ms/Pa)	Static FSS	Dynamic FSS	Combined FSS
Domain Search	5.700×10^{-8}	2.477×10^{-14}	3.132×10^{-11}	0.82	0.79	1.61
Region 1	5.665×10^{-8}	2.964×10^{-14}	6.034×10^{-11}	0.97	0.95	1.91
Region 2	5.668×10^{-8}	2.850×10^{-14}	6.306×10^{-11}	0.97	0.95	1.92
Region 3	5.672×10^{-8}	2.641×10^{-14}	6.491×10^{-11}	0.97	0.96	1.93

Table C.10: Design ranges for three experimental regions used in fitting model configured {5, 4, 3, 1}

Design	β **Min**	β **Max**	α **Min**	α **Max**	λ **Min**	λ **Max**
Region 1	5.638×10^{-8}	5.763×10^{-8}	1.477×10^{-11}	3.477×10^{-11}	5.000×10^{-11}	7.500×10^{-11}
Region 2	5.634×10^{-8}	5.696×10^{-8}	2.465×10^{-11}	3.465×10^{-11}	5.284×10^{-11}	6.784×10^{-11}
Region 3	5.652×10^{-8}	5.684×10^{-8}	2.600×10^{-11}	3.100×10^{-11}	5.931×10^{-11}	6.681×10^{-11}

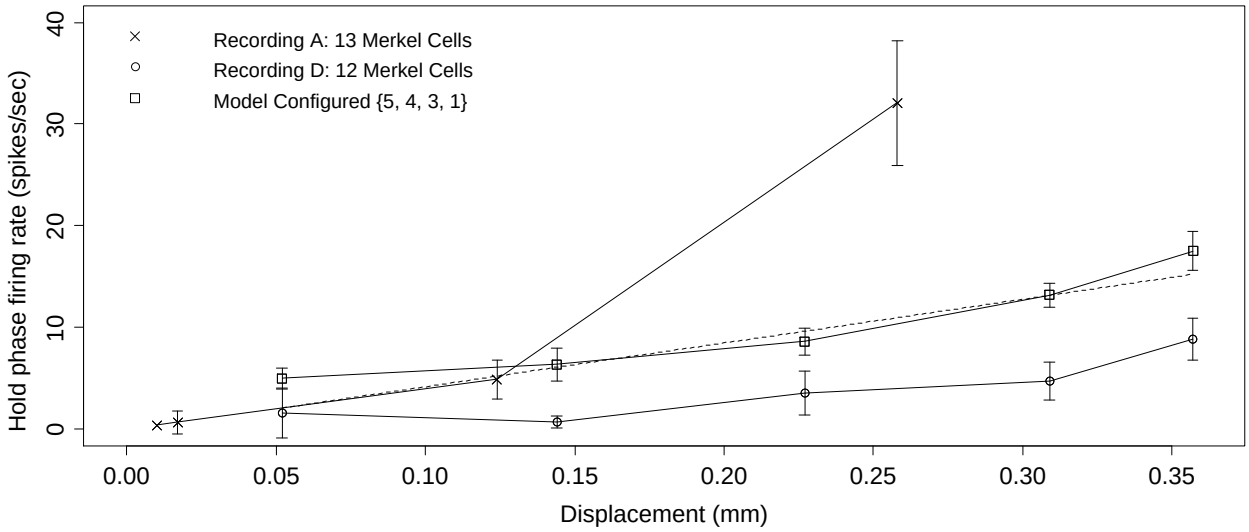

Figure C.4: Resulting displacement vs. firing rate for model configured {5, 4, 3, 1}. Note the resulting input-output relationship is in agreement with the baseline response fit to (dashed line). The most (A) and least (D) responsive SAI afferents recorded from are displayed for context, and the modeled output falls within the observed range.

References

[1] K. O. Johnson, “The roles and functions of cutaneous mechanoreceptors,” *Curr. Opin. Neurobiol.*, vol. 11, no. 4, pp. 455–461, Aug. 2001.

[2] A. Iggo and A. R. Muir, “The structure and function of a slowly adapting touch corpuscle in hairy skin,” *J Physiol*, vol. 1969/02/01, no. 3, pp. 763–96, Feb. 1969.

[3] C. J. Woodbury and H. R. Koerber, “Central and peripheral anatomy of slowly adapting type I low-threshold mechanoreceptors innervating trunk skin of neonatal mice,” *J Comp Neurol*, vol. 2007/10/11, no. 5, pp. 547–61, Dec. 2007.

[4] Johnson, K. O. and Phillips, J. R., “Tactile Spatial Resolution. I. Two-Point Discrimination, Gap Detection, Grating Resolution, and Letter Recognition,” *Journal of Neurophysiology*, vol. 46, no. 6, pp. 1177–1191, 1981.

[5] A. B. Vallbo, K. A. Olsson, K. G. Westberg, and F. J. Clark, “Microstimulation of single tactile afferents from the human hand. Sensory attributes related to unit type and properties of receptive fields,” *Brain*, vol. 107 (Pt 3), pp. 727–749, Sep. 1984.

[6] K. Zimmermann, A. Hein, U. Hager, J. S. Kaczmarek, B. P. Turnquist, D. E. Clapham, and P. W. Reeh, “Phenotyping sensory nerve endings in vitro in the mouse,” *Nat Protoc*, vol. 4, no. 2, pp. 174–196, Feb. 2009.

[7] S. A. Wellnitz, D. R. Lesniak, G. J. Gerling, and E. A. Lumpkin, “The regularity of sustained firing reveals two populations of slowly adapting touch receptors in mouse hairy skin,” *J. Neurophysiol.*, vol. 103, no. 6, pp. 3378–3388, Apr. 2010.

[8] Daine R. Lesniak, Kara L. Marshall, Scott A. Wellnitz, Blair Jenkins, Matthew Rasband, Gregory J. Gerling, and Ellen A. Lumpkin, “Neuronal Architecture Dictates Sensitivity of Mammalian Touch Receptors,” In Preparation.

[9] A. W. Goodwin and H. E. Wheat, “Effects of nonuniform fiber sensitivity, innervation geometry, and noise on information relayed by a population of slowly adapting type I primary afferents from the fingerpad,” *The Journal of Neuroscience*, vol. 19, no. 18, pp. 8057–8070, 1999.

[10] H. E. Wheat and A. W. Goodwin, “Tactile Discrimination of Gaps by Slowly Adapting Afferents: Effects of Population Parameters and Anisotropy in the Fingerpad,” *Journal of Neurophysiology.*, vol. 84, pp. 1430–1444, 2000.

[11] H. Wheat and A. Goodwin, “Tactile discrimination of edge shape: limits on spatial resolution imposed by parameters of the peripheral neural population,” *Journal of Neuroscience*, vol. 21, pp. 7751–7763, 2001.

[12] F. J. Looft and C. M. Baltensperger, “Linear-Systems Analysis of Cutaneous Type-I Mechanoreceptors,” *Ieee Transactions on Biomedical Engineering*, vol. 37, no. 6, pp. 565–573, Jun. 1990.

[13] J. R. Phillips and K. O. Johnson, “Tactile spatial resolution. III. a continuum-mechanics model of skin predicting mechanoreceptor responses to bars, edges, and gratings,” *Journal of Neurophysiology*, vol. 46, no. 6, pp. 1204–1225, 1981.

[14] A. P. Sripati, S. J. Bensmaia, and K. O. Johnson, “A continuum mechanical model of mechanoreceptive afferent responses to indented spatial patterns,” *J. Neurophysiol.*, vol. 95, no. 6, pp. 3852–3864, Jun. 2006.

[15] M. A. Srinivasan and K. Dandekar, “An investigation of the mechanics of tactile sense using two-dimensional models of the primate fingertip,” *J. Biomech. Eng.-Trans. ASME*, vol. 118, no. 1, pp. 48–55, Feb. 1996.

[16] K. Dandekar, B. I. Raju, and M. A. Srinivasan, “3-D finite-element models of human and monkey fingertips to investigate the mechanics of tactile sense,” *J. Biomech. Eng.-Trans. ASME*, vol. 125, no. 5, pp. 682–691, Oct. 2003.

[17] W. Q. Ge and P. S. Khalsa, “Encoding of compressive stress during indentation by slowly adapting type i mechanoreceptors in rat hairy skin,” *J. Neurophysiol.*, vol. 87, no. 4, pp. 1686–1693, Apr. 2002.

[18] J. Z. Wu, R. G. Dong, S. Rakheja, A. W. Schopper, and W. P. Smutz, “A structural fingertip model for simulating of the biomechanics of tactile sensation,” *Med. Eng. Phys.*, vol. 26, no. 2, pp. 165–175, Mar. 2004.

[19] J. E. Bischoff, E. M. Arruda, and K. Grosh, “Finite element modeling of human skin using an isotropic, nonlinear elastic constitutive model,” *Journal of Biomechanics*, vol. 33, no. 6, pp. 645–652, Jun. 2000.

[20] Y. Lanir, “Plausibility of Structural Constitutive-Equations for Isotropic Soft-Tissues in Finite Static Deformations,” *Journal of Applied Mechanics-Transactions of the Asme*, vol. 61, no. 3, pp. 695–702, Sep. 1994.

[21] R. Ogden, *Non-linear elastic deformations*. Mineola, NY: Dover Publications, 1997.

[22] D. T. V. Pawluk and R. D. Howe, “Dynamic lumped element response of the human fingerpad,” *Journal of Biomechanical Engineering - Transactions of the ASME*, vol. 121, pp. 178–183, 1999.

[23] W. Gerstner and W. M. Kistler, *Spiking Neuron Models: Single Neurons, Populations, and Plasticity*. Cambridge, UK: Cambridge University Press, 2002.

[24] E. M. Izhikevich, “Which model to use for cortical spiking neurons?,” *IEEE Trans. Neural Netw.*, vol. 15, no. 5, pp. 1063–1070, 2004.

[25] E. M. Izhikevich, “Simple model of spiking neurons,” *IEEE Trans. Neural Netw.*, vol. 14, no. 6, pp. 1569–1572, Nov. 2003.

[26] S. Bensmaia, “A transduction model of the meissner corpuscle,” *Math. Biosci.*, vol. 176, no. 2, pp. 203–217, Apr. 2002.

[27] A. W. Freeman and K. O. Johnson, “Cutaneous mechanoreceptors in macaque monkey - temporal discharge patterns evoked by vibration, and a receptor model,” *Journal of Physiology-London*, vol. 323, pp. 21–41, 1982.

[28] A. W. Freeman and K. O. Johnson, “A model accounting for effects of vibratory amplitude on responses of cutaneous mechanoreceptors in macaque monkey,” *J. Physiol.-London*, vol. 323, no. FEB, pp. 43–64, 1982.

[29] Y. Y. Leung, S. J. Bensmaia, S. S. Hsiao, and K. O. Johnson, “Time-course of vibratory adaptation and recovery in cutaneous mechanoreceptive afferents,” *J. Neurophysiol.*, vol. 94, no. 5, pp. 3037–3045, Nov. 2005.

[30] S. J. Bensmaia, Y. Y. Leung, S. S. Hsiao, and K. O. Johnson, “Vibratory adaptation of cutaneous mechanoreceptive afferents,” *J. Neurophysiol.*, vol. 94, no. 5, pp. 3023–3036, Nov. 2005.

[31] D. R. Lesniak and G. J. Gerling, “Predicting SA-I mechanoreceptor spike times with a skin-neuron model,” *Math. Biosci.*, vol. 220, no. 1, pp. 15–23, Jul. 2009.

[32] R. S. Johansson, U. Landstrom, and R. Lundstrom, “Sensitivity to Edges of Mechanoreceptive Afferent Units Innervating the Glabrous Skin of the Human Hand,” *Brain Res.*, vol. 244, no. 1, pp. 27–32, 1982.

[33] J. R. Phillips and K. O. Johnson, “Tactile spatial resolution. II. neural representation of bars, edges, and gratings in monkey primary afferents,” *Journal of Neurophysiology*, vol. 46, no. 6, pp. 1192–1203, 1981.

[34] R. S. Johansson and A. B. Vallbo, “Skin Mechanoreceptors in the Human Hand: An Inference of Some Population Properties,” in *Sensory Functions of the Skin*, 1st edition., Pergamon Press.

[35] M. A. Serrat, C. I. Vinyard, and D. King, “Alterations in the mechanical properties and composition of skin in human growth hormone transgenic mice,” *Connect. Tissue Res.*, vol. 48, no. 1, pp. 19–26, 2007.

[36] H. Haeberle and E. A. Lumpkin, “Merkel Cells in Somatosensation,” *Chemosensory Perception*, vol. 1, no. 2, pp. 110–118, Jun. 2008.

[37] D. Guinard, Y. Usson, C. Guillermet, and R. Saxod, “Merkel complexes of human digital skin: Three-dimensional imaging with confocal laser microscopy and double immunofluorescence,” *J. Comp. Neurol.*, vol. 398, no. 1, pp. 98–104, Aug. 1998.

[38] K. W. Horch, D. Whitehorn, and P. R. Burgess, “Impulse generation in type I cutaneous mechanoreceptors,” *J. Neurophysiol.*, vol. 37, no. 2, pp. 267–281, Mar. 1974.

[39] J. R. Phillips and K. O. Johnson, “Tactile spatial resolution. III. A continuum mechanics model of skin predicting mechanoreceptor responses to bars, edges, and gratings,” *J. Neurophysiol.*, vol. 46, no. 6, pp. 1204–25, 1981.

[40] G. J. Gerling and G. W. Thomas, “Fingerprint lines may not directly affect SA-I mechanoreceptor response,” *Somatosens. Mot. Res.*, vol. 25, no. 1, pp. 61–76, 2008.

[41] W. H. Press, Ed., *Numerical recipes in C : the art of scientific computing /*, 2nd ed. Cambridge [Cambridgeshire] ;: Cambridge University Press,, 1992.

[42] F. Rugiero, L. J. Drew, and J. N. Wood, “Kinetic properties of mechanically activated currents in spinal sensory neurons,” *The Journal of Physiology*, vol. 588, no. 2, pp. 301–314, Nov. 2009.

[43] J. R. Holt and D. P. Corey, “Two mechanisms for transducer adaptation in vertebrate hair cells,” *Proc. Natl. Acad. Sci.*, vol. 97, no. 22, pp. 11730–11735, Oct. 2000.

[44] J. Siemens, S. Zhou, R. Piskorowski, T. Nikai, E. A. Lumpkin, A. I. Basbaum, D. King, and D. Julius, “Spider toxins activate the capsaicin receptor to produce inflammatory pain,” *Nature*, vol. 444, no. 7116, pp. 208–212, 2006.

[45] S. Crino and D. E. Brown, “Global optimization with multivariate adaptive regression splines,” *IEEE Trans Syst Man Cybern B Cybern*, vol. 37, no. 2, pp. 333–340, Apr. 2007.

[46] B. GüÇlü, G. K. Mahoney, L. J. Pawson, A. K. Pack, R. L. Smith, and S. J. Bolanowski, “Localization of Merkel cells in the monkey skin: An anatomical model,” *Somatosensory & Motor Research*, vol. 25, no. 2, pp. 123–138, Jan. 2008.

[47] J. P. Eagles and R. L. Purple, “Afferent fibers with multiple encoding sites,” *Brain Research*, vol. 77, no. 2, pp. 187–193, Sep. 1974.

[48] J. G. Nicholls, A. R. Martin, B. G. Wallace, and Fuchs, *From Neuron to Brain: A Cellular and Molecular Approach to the Function of the Nervous System*, 4th ed. Sunderland Mass.: Sinauer Associates, 2001.

[49] R. W. Banks, M. Hulliger, K. A. Scheepstra, and E. Otten, “Pacemaker activity in a sensory ending with multiple encoding sites: the cat muscle spindle primary ending,” *J. Physiol. (Lond.)*, vol. 498 (Pt 1), pp. 177–199, Jan. 1997.

[50] D. C. Quick, W. R. Kennedy, and R. E. Poppele, “Anatomical evidence for multiple sources of action potentials in the afferent fibers of muscle spindles,” *Neuroscience*, vol. 5, no. 1, pp. 109–115, Jan. 1980.

[51] D. H.-E., R. F., and B. F., “Arthropod touch reception: stimulus transformation and finite element model of spider tactile hairs,” *Journal of Comparative Physiology A: Sensory, Neural, and Behavioral Physiology*, vol. 187, no. 4, pp. 313–322, May 2001.

[52] B. GüÇlü, E. A. Schepis, S. Yelke, C. A. Yucesoy, and S. J. Bolanowski, “Ovoid geometry of the Pacinian corpuscle is not the determining factor for mechanical excitation,” *Somatosensory & Motor Research*, vol. 23, no. 3–4, pp. 119–126, Jan. 2006.

[53] D. T. V. Pawluk and R. Howe, “A Holistic Model of Human Touch,” in *Computational Neuroscience: Trends in Research*, New York: Plenum Press, 1997, pp. 759–764.

[54] S. M. Maricich, S. A. Wellnitz, A. M. Nelson, D. R. Lesniak, G. J. Gerling, E. A. Lumpkin, and H. Y. Zoghbi, “Merkel Cells Are Essential for Light-Touch Responses,” *Science*, vol. 324, no. 5934, pp. 1580–1582, Jun. 2009.

[55] Kara L. Marshall and Ellen A. Lumpkin, “The SAI End Organ Remodels with the Hair Cycle and Simplifies With Age,” *Unpublished*, In Preparation.

[56] S. Müller-Röver, B. Handjiski, C. van der Veen, S. Eichmüller, K. Foitzik, I. A. McKay, K. S. Stenn, and R. Paus, “A comprehensive guide for the accurate classification of murine hair follicles in distinct hair cycle stages,” *J. Invest. Dermatol.*, vol. 117, no. 1, pp. 3–15, Jul. 2001.

[57] Yuxiang Wang, “Impact of skin hyper- and visco-elasticity on neural mechanotransduction of the slowly adapting type I afferent,” MS, University of Virginia, 2012.

[58] M. V. Plikus and C.-M. Chuong, “Complex Hair Cycle Domain Patterns and Regenerative Hair Waves in Living Rodents,” *Journal of Investigative Dermatology*, vol. 128, no. 5, pp. 1071–1080, May 2008.

[59] M. V. Plikus, J. A. Mayer, D. de la Cruz, R. E. Baker, P. K. Maini, R. Maxson, and C.-M. Chuong, “Cyclic dermal BMP signalling regulates stem cell activation during hair regeneration,” *Nature*, vol. 451, no. 7176, pp. 340–344, Jan. 2008.

[60] K. I. Baumann, W. Hamann, and M. S. Leung, “Mechanical-properties of skin and responsiveness of slowly adapting type-I mechanoreceptors in rats at different ages,” *J. Physiol.-London*, vol. 371, pp. 329–337, Feb. 1986.

[61] M. V. Srinivasan, “Visual control of navigation in insects and its relevance for robotics,” *Current Opinion in Neurobiology*, vol. 21, no. 4, pp. 535–543, Aug. 2011.

[62] J. H. Solomon and M. J. Z. Hartmann, “Extracting Object Contours with the Sweep of a Robotic Whisker Using Torque Information,” *The International Journal of Robotics Research*, vol. 29, no. 9, pp. 1233–1245, May 2009.

[63] D. Yamada, T. Maeno, and Y. Yamada, “Artificial finger skin having ridges and distributed tactile sensors used for grasp force control,” *J. Robot. Mech.*, vol. 14, no. 2, pp. 140–146, 2002.

[64] J. Scheibert, S. Leurent, A. Prevost, and G. Debregeas, “The role of fingerprints in the coding of tactile information probed with a biomimetic sensor,” *Science*, vol. 323, no. 5920, pp. 1503–1506, Mar. 2009.

[65] S. J. Thorpe, R. Guyonneau, N. Guilbaud, J.-M. Allegraud, and R. VanRullen, “SpikeNet: real-time visual processing with one spike per neuron,” *Neurocomputing*, vol. 58–60, pp. 857–864, Jun. 2004.

[66] S. S. Kim, A. P. Sripati, R. J. Vogelstein, R. S. Armiger, A. F. Russell, and S. J. Bensmaia, “Conveying tactile feedback in sensorized hand neuroprostheses using a biofidelic model of mechanotransduction,” *IEEE Trans. Biomed. Circuits Syst.*, vol. 3, no. 6, pp. 398–404, Dec. 2009.

[67] E. Kim, S. M. Bourdon, S. A. Wellnitz, E. A. Lumpkin, and G. J. Gerling, “Force sensor in simulated skin and neural model mimic tactile SAI afferent spiking response to ramp and hold stimuli,” *Journal of NeuroEngineering and Rehabilitation*, vol. 9, no. 1, p. 45, 2012.

[68] B. Guclu, “Location of Merkel cells in the monkey skin: An anatomical model,” *Somatosensory and Motor Research*, vol. 25, no. 2, pp. 123–138, Jun. 2008.

[69] A. W. Goodwin and H. E. Wheat, “Sensory signals in neural populations underlying tactile perception and manipulation,” *Annu. Rev. Neurosci.*, vol. 27, pp. 53–77, 2004.

[70] Gregory J. Gerling, Isabelle I. Rivest, Daine R. Lesniak, Jacob R. Scanlon, and Lingtian Wan, “Validating a Population Model of Tactile Mechanotransduction of Slowly Adapting Type I Afferents at Levels of Skin Mechanics, Single-unit Response and Psychophysics,” *IEEE Transactions on Haptics*, In Preparation.

[71] Y. Fukami, “Interaction of impulse activities originating from individual Golgi tendon organs innervated by branches of a single axon,” *J Physiol*, vol. 1980/01/01, pp. 483–99, Jan. 1980.

[72] R. W. Banks, M. Hulliger, H. H. Saed, and M. J. Stacey, “A comparative analysis of the encapsulated end-organs of mammalian skeletal muscles and of their sensory nerve endings,” *J Anat*, vol. 2009/06/23, no. 6, pp. 859–87, Jun. 2009.

[73] A. L. Williams, G. J. Gerling, S. A. Wellnitz, and E. A. Lumpkin, “Skin relaxation predicts neural firing rate adaptation in sai touch receptors,” in *Proceedings of the 32nd Annual International Conference of the IEEE EMBS*, Buenos Aires, Argentina, 2010, pp. 6678–6681.

[74] E. K. Kim, G. J. Gerling, S. A. Wellnitz, and E. A. Lumpkin, “Using Force Sensors and Neural Models to Encode Tactile Stimuli as Spike-based Responses,” *Proceedings of the 2010 IEEE Haptic Interfaces for Virtual Environment and Teleoperator Systems conference, in review*, 2009.

[75] D. R. Lesniak, G. J. Gerling, S. A. Wellnitz, and E. A. Lumpkin, “Statistical analysis and modeling of variance in the SA-I mechanoreceptor response to sustained indentation,” in *IEEE Engineering in Medicine and Biology Society (31st Annual)*, 2009, vol. Minneapolis, MN, pp. 6814–6817.